

## EXTRAGALACTIC MILLIMETER-WAVE SOURCES IN SOUTH POLE TELESCOPE SURVEY DATA: SOURCE COUNTS, CATALOG, AND STATISTICS FOR AN 87 SQUARE-DEGREE FIELD

J. D. VIEIRA<sup>1,2,3</sup>, T. M. CRAWFORD<sup>1,4</sup>, E. R. SWITZER<sup>1</sup>, P. A. R. ADE<sup>5</sup>, K. A. AIRD<sup>6</sup>, M. L. N. ASHBY<sup>7</sup>, B. A. BENSON<sup>1</sup>, L. E. BLEEM<sup>1,2</sup>, M. BRODWIN<sup>7,25</sup>, J. E. CARLSTROM<sup>1,2,3,4</sup>, C. L. CHANG<sup>1,3</sup>, H.-M. CHO<sup>8</sup>, A. T. CRITES<sup>1,4</sup>, T. DE HAAN<sup>9</sup>, M. A. DOBBS<sup>9</sup>, W. EVERETT<sup>6</sup>, E. M. GEORGE<sup>8</sup>, M. GLADDERS<sup>1,4</sup>, N. R. HALL<sup>10</sup>, N. W. HALVERSON<sup>11</sup>, F. W. HIGH<sup>12</sup>, G. P. HOLDER<sup>9</sup>, W. L. HOLZAPFEL<sup>8</sup>, J. D. HRUBES<sup>6</sup>, M. JOY<sup>13</sup>, R. KEISLER<sup>1,2,3</sup>, L. KNOX<sup>10</sup>, A. T. LEE<sup>8,14</sup>, E. M. LEITCH<sup>1,4</sup>, M. LUEKER<sup>8</sup>, D. P. MARRONE<sup>1,26</sup>, V. MCINTYRE<sup>15</sup>, J. J. MCMAHON<sup>1,3,16</sup>, J. MEHL<sup>1</sup>, S. S. MEYER<sup>1,2,3,4</sup>, J. J. MOHR<sup>17,18,19</sup>, T. E. MONTROY<sup>20,21</sup>, S. PADIN<sup>1,4</sup>, T. PLAGGE<sup>1,8</sup>, C. PRYKE<sup>1,3,4</sup>, C. L. REICHARDT<sup>8</sup>, J. E. RUHL<sup>20,21</sup>, K. K. SCHAFFER<sup>1,3</sup>, L. SHAW<sup>9,22</sup>, E. SHIROKOFF<sup>8</sup>, H. G. SPIELER<sup>14</sup>, B. STALDER<sup>7</sup>, Z. STANISZEWSKI<sup>20,21</sup>, A. A. STARK<sup>7</sup>, K. VANDERLINDE<sup>9</sup>, W. WALSH<sup>7</sup>, R. WILLIAMSON<sup>6</sup>, Y. YANG<sup>23</sup>, O. ZAHN<sup>24</sup>, AND A. ZENTENO<sup>23</sup>

<sup>1</sup> Kavli Institute for Cosmological Physics, University of Chicago, 5640 South Ellis Avenue, Chicago, IL 60637, USA; [vieira@caltech.edu](mailto:vieira@caltech.edu)

<sup>2</sup> Department of Physics, University of Chicago, 5640 South Ellis Avenue, Chicago, IL 60637, USA

<sup>3</sup> Enrico Fermi Institute, University of Chicago, 5640 South Ellis Avenue, Chicago, IL 60637, USA

<sup>4</sup> Department of Astronomy and Astrophysics, University of Chicago, 5640 South Ellis Avenue, Chicago, IL 60637, USA

<sup>5</sup> Department of Physics and Astronomy, Cardiff University, CF24 3YB, UK

<sup>6</sup> University of Chicago, 5640 South Ellis Avenue, Chicago, IL 60637, USA

<sup>7</sup> Harvard-Smithsonian Center for Astrophysics, 60 Garden Street, Cambridge, MA 02138, USA

<sup>8</sup> Department of Physics, University of California, Berkeley, CA 94720, USA

<sup>9</sup> Department of Physics, McGill University, 3600 Rue University, Montreal, Quebec H3A 2T8, Canada

<sup>10</sup> Department of Physics, University of California, One Shields Avenue, Davis, CA 95616, USA

<sup>11</sup> Department of Astrophysical and Planetary Sciences and Department of Physics, University of Colorado, Boulder, CO 80309, USA

<sup>12</sup> Department of Physics, Harvard University, 17 Oxford Street, Cambridge, MA 02138, USA

<sup>13</sup> Department of Space Science, VP62, NASA Marshall Space Flight Center, Huntsville, AL 35812, USA

<sup>14</sup> Physics Division, Lawrence Berkeley National Laboratory, Berkeley, CA 94720, USA

<sup>15</sup> Australia Telescope National Facility, CSIRO, Epping, NSW 1710, Australia

<sup>16</sup> Department of Physics, University of Michigan, 450 Church Street, Ann Arbor, MI 48109, USA

<sup>17</sup> Department of Physics, Ludwig-Maximilians-Universität, Scheinerstr. 1, 81679 München, Germany

<sup>18</sup> Excellence Cluster Universe, Boltzmannstrasse 2, 85748 Garching, Germany

<sup>19</sup> Max-Planck-Institut für extraterrestrische Physik, Giessenbachstr. 85748 Garching, Germany

<sup>20</sup> Physics Department, Case Western Reserve University, Cleveland, OH 44106, USA

<sup>21</sup> Center for Education and Research in Cosmology and Astrophysics, Case Western Reserve University, Cleveland, OH 44106, USA

<sup>22</sup> Department of Physics, Yale University, P.O. Box 208210, New Haven, CT 06520-8120, USA

<sup>23</sup> Department of Astronomy and Department of Physics, University of Illinois, 1002 West Green Street, Urbana, IL 61801, USA

<sup>24</sup> Berkeley Center for Cosmological Physics, Department of Physics, University of California, and Lawrence Berkeley National Labs, Berkeley, CA 94720, USA

Received 2009 December 11; accepted 2010 June 22; published 2010 July 22

### ABSTRACT

We report the results of an 87 deg<sup>2</sup> point-source survey centered at R.A. 5<sup>h</sup>30<sup>m</sup>, decl. –55° taken with the South Pole Telescope at 1.4 and 2.0 mm wavelengths with arcminute resolution and milli-Jansky depth. Based on the ratio of flux in the two bands, we separate the detected sources into two populations, one consistent with synchrotron emission from active galactic nuclei and the other consistent with thermal emission from dust. We present source counts for each population from 11 to 640 mJy at 1.4 mm and from 4.4 to 800 mJy at 2.0 mm. The 2.0 mm counts are dominated by synchrotron-dominated sources across our reported flux range; the 1.4 mm counts are dominated by synchrotron-dominated sources above ~15 mJy and by dust-dominated sources below that flux level. We detect 141 synchrotron-dominated sources and 47 dust-dominated sources at signal-to-noise ratio S/N > 4.5 in at least one band. All of the most significantly detected members of the synchrotron-dominated population are associated with sources in previously published radio catalogs. Some of the dust-dominated sources are associated with nearby ( $z \ll 1$ ) galaxies whose dust emission is also detected by the *Infrared Astronomy Satellite*. However, most of the bright, dust-dominated sources have no counterparts in any existing catalogs. We argue that these sources represent the rarest and brightest members of the population commonly referred to as submillimeter galaxies (SMGs). Because these sources are selected at longer wavelengths than in typical SMG surveys, they are expected to have a higher mean redshift distribution and may provide a new window on galaxy formation in the early universe.

**Key words:** galaxies: high-redshift – submillimeter: galaxies – surveys

*Online-only material:* machine-readable table

### 1. INTRODUCTION

The 10 m South Pole Telescope (SPT; Carlstrom et al. 2009) is a millimeter/submillimeter (mm/submm) telescope

located at the geographic South Pole and designed for low-noise observations of diffuse, low-contrast sources such as anisotropy in the cosmic microwave background (CMB). The first camera installed on the SPT is a 960-element bolometric receiver designed to perform a mass-limited survey of galaxy clusters via their Sunyaev–Zel’dovich (SZ) signature (Sunyaev & Zeldovich 1972) over a large area of the southern sky. This survey is

<sup>25</sup> W. M. Keck Postdoctoral Fellow at the Harvard-Smithsonian Center for Astrophysics

<sup>26</sup> Jansky Fellow, National Radio Astronomy Observatory

currently underway and the SPT team recently published the first-ever discovery of galaxy clusters through their SZ signature (Staniszewski et al. 2009, hereafter S09).

The sensitivity and angular resolution of the SPT make it an excellent instrument for detecting extragalactic sources of emission. In this work, we report on source detections in a small part of the SPT survey, namely a single 87 deg<sup>2</sup> field centered at R.A. 5<sup>h</sup>30<sup>m</sup>, decl. −55° (J2000). This field was surveyed by the SPT in the 2008 season to roughly mJy depth at 1.4 mm and 2.0 mm (220 and 150 GHz). The data presented here represent a major step forward in mm source detection at these flux levels, both in area surveyed and in the ability to distinguish between source populations using internal estimates of source spectral properties.

Simultaneous information in two bands for each detected source should allow us to separate our detections into distinct source populations. Based on previous surveys at mm wavelengths and on surveys in neighboring centimeter (cm) and submm bands, we expect the sources we detect to fall into two broad categories: (1) sources with flat or decreasing brightness with decreasing wavelength, consistent with synchrotron emission from active galactic nuclei (AGNs, typically  $S \propto \lambda^{-1}$ ) and (2) sources with increasing brightness with decreasing wavelength, consistent with thermal emission (typically  $S \propto \lambda^{-3}$ ) from dust-enshrouded star-forming galaxies.

The synchrotron-dominated source population is well established from radio surveys (see De Zotti et al. 2010 for a recent review). Despite these sources' decreasing brightness from radio to mm wavelengths, simple extrapolations of radio and cm counts of these sources to the SPT bands predict that we should detect a significant number of these sources. This prediction is bolstered by the results of 3 mm follow-up of sources detected at 1.5 cm presented in Sadler et al. (2008), which showed that these sources are still emitting strongly at mm wavelengths, and by detections of synchrotron-dominated AGN emission made in mm/submm surveys much smaller than the SPT survey but at similar depths (Voss et al. 2006). Measurements of the mm fluxes of a large sample of these sources have the power to inform both astrophysical models of their emission and predictions for the extent of their contamination to the CMB power spectrum (e.g., Toffolatti et al. 2005; Reichardt et al. 2009) and the SZ signal from galaxy clusters (e.g., Lin & Mohr 2007; Sehgal et al. 2010).

The dust-enshrouded star-forming galaxy population has been the subject of considerable interest for over thirty years (see Rieke & Lebofsky 1979 for a pre-*IRAS* review), but the *Infrared Astronomy Satellite* (*IRAS*) was the first instrument to systematically discover such objects (Sanders & Mirabel 1996). Optical and UV observations show these sources to be heavily dust-obscured, and to typically have disturbed morphologies and high star formation rates, indicative of recent or ongoing mergers (Lagache et al. 2005). The emission from IR to mm wavelengths in these sources arises from short-wavelength photons emitted by stars, which are absorbed by dust grains and re-radiated at longer wavelengths (Draine 2003).

Measurements of the cosmic infrared background (CIB) show that over half of the energy emitted since the surface of last scattering has been absorbed and re-radiated by dust (Dwek et al. 1998). *IRAS*, however, detected mostly low-redshift ( $z < 1$ ) objects, and these relatively rare and nearby sources contributed only a small fraction of the CIB (Le Flocc'h et al. 2005; Caputi et al. 2007), indicating that the bulk of CIB sources are at high redshift. The first systematic survey of high-redshift sources that

contribute significantly to the CIB—the population now known as submillimeter galaxies (SMGs)—was carried out a decade ago at 850  $\mu\text{m}$  by the SCUBA instrument on the 15 m James Clerk Maxwell Telescope (Smail et al. 1997; Hughes et al. 1998; Barger et al. 1998; Holland et al. 1999). Owing to the spectrum of SMGs—a modified  $\sim 30$  K blackbody that rises steeply with decreasing wavelength, counteracting the expected flux diminution with redshift—they can be detected independently of redshift from roughly 500  $\mu\text{m}$  to 2 mm (Blain et al. 2002). This implies that the source luminosity is roughly proportional to the brightness from  $1 < z < 10$ .

Hundreds of SMGs have now been detected by ground-based telescopes in surveys of blank fields, but only over a total area on the order of a square degree (Scott et al. 2002; Borys et al. 2003; Greve et al. 2004; Laurent et al. 2005; Coppin et al. 2006; Bertoldi et al. 2007; Perera et al. 2008; Scott et al. 2008; Austermann et al. 2010; Weiß et al. 2009). Recently, results were published from the Balloon-borne Large-aperture Submillimeter Telescope which surveyed nearly 10 deg<sup>2</sup> at 250, 350, and 550  $\mu\text{m}$  and measured important properties such as dust temperatures and clustering amplitude for SMGs (Devlin et al. 2009; Patanchon et al. 2009; Dye et al. 2009; Viero et al. 2009). The discovery and study of SMGs has revolutionized our understanding of galaxy formation by providing a view of galaxy formation which is both unbiased with redshift and inaccessible to optical surveys. Observations of these objects (see Blain et al. (2002) for a review) indicate that: (1) they have dynamical masses of  $\sim 10^{11} M_{\odot}$  and total far-infrared luminosities of  $\sim 10^{13} L_{\odot}$  (Swinbank et al. 2004; Greve et al. 2005; Chapman et al. 2005; Kovács et al. 2006; Pope et al. 2006); (2) they are forming stars prodigiously at  $\sim 1000 M_{\odot} \text{ yr}^{-1}$  (Chapman et al. 2005; Tacconi et al. 2006); (3) their abundance appears to peak at  $z \sim 2.5$  (Pope et al. 2005; Chapman et al. 2005; Aretxaga et al. 2007; Chapin et al. 2009); (4) from observations (Tacconi et al. 2008) and simulation (Barnes & Hernquist 1991; Narayanan et al. 2010), the prodigious star formation rate seen in SMGs is believed to be intrinsically linked to mergers; and (5) SMGs are an early phase in the formation of the most massive galaxies and are among the largest gravitationally collapsed objects in this early epoch of galaxy formation (Blain et al. 2004; Swinbank et al. 2008).

In the context of this broad field of IR/submm/mm-selected, dust-enshrouded, star-forming galaxies, this paper presents the detection in the SPT data of a population of dust-dominated sources with surprising and intriguing properties. These sources are significantly brighter and rarer than the submm-selected population in the literature. Furthermore, the majority of these sources do not have counterparts in *IRAS* indicating that they are not members of the standard local ultra-luminous infrared galaxy (ULIRG) population. This apparently new family of sources represents the most significant new result of this work.

This paper is divided into several sections. Section 2 describes the SPT observations, data reduction, matched filter for point-source signal, and source-finding algorithm. (The observations and data reduction through the map-making step are described in more detail in S09 and Carlstrom et al. 2009.) Section 3 discusses the properties of the filtered maps, presents the source catalog, describes our procedures for checking astrometry and estimating completeness and purity, and discusses basic source properties, including raw spectral classification. Section 4 describes our procedure for estimating each source's intrinsic flux and spectral index, which we use to separate our sources into two spectrally distinct (synchrotron-dominated and dust-dominated) populations. The statistical method used for flux estimation is

described in detail in a companion paper, Crawford et al. (2010). Section 5 presents source counts for each band. Section 6 discusses associations with external catalogs. Finally, Section 7 presents counts for each of the populations and discusses the implications, including the potential for a newly discovered population of sources.

In another companion paper (Hall et al. 2010), we present the spatial power spectra of the sources below our detection threshold.

## 2. OBSERVATIONS, DATA REDUCTION, AND SOURCE FINDING

This work is based on observations of a single  $\sim 100$  deg<sup>2</sup> field. The timestream data for each observation, constituting a single pass over the field, were processed and combined to make a map of the field for each observing band. The maps from several hundred individual observations of the field were combined and converted to CMB fluctuation temperature units using a calibration from the CMB anisotropy as measured by the *Wilkinson Microwave Anisotropy Probe* (*WMAP*; Hinshaw et al. 2009). Each single-band map is filtered to optimize point-source detection. A variant of the CLEAN algorithm (Högbom 1974) was then used to search for sources in an 87 deg<sup>2</sup> sub-region of the filtered maps. Finally, amplitudes of the detected peaks in the filtered maps were converted from CMB fluctuation temperature units to flux (in units of Jy).

### 2.1. Observations

During the 2008 observing season, the 960-element SPT camera included detectors sensitive to radiation within bands centered at approximately 1.4 mm, 2.0 mm, and 3.2 mm (220 GHz, 150 GHz, and 95 GHz). The first field mapped to the targeted survey depth was centered at R.A. 5<sup>h</sup>30<sup>m</sup>, decl.  $-55^\circ$  (J2000). Results in this paper are based on 607 hr of observing time, using only the 1.4 mm and 2.0 mm data from the 87 deg<sup>2</sup> portion of the field that was mapped with near-uniform coverage. (Every 1' patch in the included area is required to have uniform coverage to 10%.) The scanning strategy consisted of constant-elevation scans across the 10° wide field. After each single scan back and forth across the field, the telescope executes a 0.125 step in elevation. A complete set of scans covering the entire field takes approximately 2 hr and we refer to each complete set as an observation. Between individual observations of the field, we perform a series of short calibration measurements, including measurements of a chopped thermal source, 2° elevation nods, and scans across the galactic H II regions RCW38 and MAT5a. This series of regular calibration measurements allows us to identify detectors with good performance, assess relative detector gains, monitor atmospheric opacity and beam parameters, and constrain pointing variations. S09 and Carlstrom et al. (2009) describe details of the observations of this field and the telescope.

### 2.2. Data Reduction

The reduction of SPT data for this work up to and including the map-making step is very similar to the reduction pipeline used to produce the maps used in S09, where details of the analysis can be found. Broadly, the pipeline consists of filtering the time-ordered data from each individual detector, reconstructing the pointing for each detector, and combining data from all detectors in a given observing band into a map by simple inverse-variance-weighted binning and averaging.

The filtering used in this analysis differ from that in S09. In this work, the time-ordered detector data were filtered with a 0.18 Hz Fourier-domain high-pass filter. With our scan speeds, the high pass filter removes spatial scales  $\gtrsim 45'$ . We project out a common mode which consists of three spatial modes (mean and tilts along two axes) constructed from the mean of all working detectors in a single band, weighted by the  $x$ - and  $y$ -positions in the focal plane. As atmospheric signal is highly correlated between detectors, removing this common mode should eliminate the majority of the atmospheric fluctuation power in the detector timestreams. The common-mode subtraction acts as a spatial high-pass filter with a characteristic scale that roughly corresponds to the 1° angular field of view of the array. This filter option was demonstrated to remove more atmosphere from the timestream than the method described in S09, but its choice was not critical. As the common mode is constructed independently for each band, the response to large spatial modes on the sky can be slightly different between bands, but these modes are heavily de-weighted in the filter we later apply to the maps to enhance point-source signal-to-noise (S/N). Finally, in contrast to S09, we did not mask bright point sources when filtering the time-ordered data because we wanted to ensure that the filter transfer function would be the same for all sources in the maps.

### 2.3. Flux Calibration and Beam Measurements

The relative gains of the detectors and their gain variations over time were estimated using measurements of their response to a chopped thermal source. (These measurements took place before each observation of the survey field, or every 2 hr.) This was the same relative calibration method used in S09. The absolute calibration is based on the comparison of SPT measurements of degree-scale CMB fluctuations at 2.0 mm directly to the *WMAP* 5-year maps. This was done using short, dedicated observations of four large fields, totaling 1250 deg<sup>2</sup>. Details of the cross-calibration with *WMAP* are given in Lueker et al. (2010). We estimate the uncertainty of this calibration to be 3.6%. We applied this calibration to our 1.4 mm band by comparing 2.0 mm and 1.4 mm estimates of CMB anisotropy in our deep survey regions. This internal cross-calibration for 1.4 mm is consistent with a direct absolute calibration from RCW38, but with higher precision. We estimate the 1.4 mm calibration uncertainty to be 7.2%. Because the 1.4 mm calibration is derived from the 2.0 mm calibration to *WMAP*, the calibration uncertainties in the two bands are correlated with an estimated correlation coefficient of roughly 0.5.

Main-lobe beams were measured using the brightest sources in the field and are adequately fit by two-dimensional Gaussians with FWHM equal to 1'.05 and 1'.15 at 1.4 mm and 2.0 mm. Large-angle sidelobes were measured using planet observations, but the angular scales on which these sidelobes are important are heavily downweighted in the filter. We estimate that beam-shape uncertainties contribute roughly 2% and 5% to the absolute flux estimates in our 2.0 mm and 1.4 mm bands. This uncertainty was added in quadrature to the calibration uncertainty in our flux estimates. A visual representation of the SPT 2.0 mm beam is shown in Padin et al. (2008) and symmetrized  $\ell$ -space profiles for the beams at both wavelengths are shown in Lueker et al. (2010).

A subtlety in estimating the spectral index (Equation (5)) is that the effective band centers (which fold into the index determination) depend upon spectral index. Using the measured passbands for 1.4 mm and 2.0 mm, we find that if one were

to assume an index  $\alpha = -1$  in the determination of the band centers, a source with  $\alpha = 3$  would be measured with a 2% bias in the spectral index. In addition, the beam shape (and so flux) will change with the spectral index. These subtleties can both be neglected to the accuracy of the results presented here.

## 2.4. Source Extraction

### 2.4.1. Matched Filter

We enhanced the point-source S/N in the SPT maps by applying a matched spatial filter (see, e.g., Tegmark & de Oliveira-Costa 1998) to each single-band map. The matched filter combines knowledge of the instrument beam and any other filtering that has been performed on the data with an estimate of noise covariance to optimize the S/N of a source in the filtered map. This matched filter  $\psi$  is applied in the Fourier domain and is given by

$$\psi \equiv \frac{\tau^T N^{-1}}{\sqrt{\tau^T N^{-1} \tau}}, \quad (1)$$

where  $N$  is the noise covariance matrix (including astrophysical contaminants such as primary CMB anisotropy) and  $\tau$  is the assumed source shape in the map, which in the case of point sources is a function of beam and filtering only. Real-space visual representations of  $\tau$  for 1.4 mm and 2.0 mm—with filtering very similar to that used in the maps in this work—are shown in Plagge et al. (2010).

As in S09, the instrumental and atmospheric contributions to the noise covariance in each band were estimated by computing the average power spectrum of hundreds of signal-free maps, constructed by multiplying half of the 320 individual-observation maps of the field by  $-1$ , half by  $+1$ , and then summing. (Hereafter, this will be referred to as the “difference” map, in which all astrophysical signal has been removed from the map, but the atmospheric and detector noise remains.) The main astrophysical contribution to the noise covariance is expected to be primary CMB anisotropy, so an estimate of the CMB power spectrum was added to the noise covariance. Adding further astrophysical contributions such as the SZ background and point sources below our detection threshold has a negligible effect on our results.

The source shape used in the matched filter is the convolution of our measured beam and the map-domain equivalent of any timestream filtering that we have performed. We measured the effect of timestream filtering on the expected shape of point sources in our maps by performing signal-only simulations of our data processing, using a single model point source projected into our detector timestreams as the only timestream component.

Observations used here were performed using constant declination scans. The maps were pixelized using a flat-sky projection of the sphere in which the mapping of R.A. to map rows is a function of position in the map.<sup>27</sup> As a result, the effects of timestream filtering on source shape are also map-position dependent. To account for this, we break the single-band co-added signal maps into nine tiles and perform our signal-only simulations nine times—once with the model source located at the center of each tile. We broke the map into nine tiles (as opposed to four or sixteen) as it solved the problem with the greatest economy. We estimated the noise covariance separately for each tile, as the projection of non-white timestream noise into the map is also a function of the position. The noise in

the outer tiles is within 5% of the noise in the center tile (see Section 3). We constructed nine matched filters from these inputs and performed source finding on each map tile individually with the matched filter constructed from that tile’s inputs.

### 2.4.2. Candidate Identification

Source candidates were identified in the filtered maps using a variant of the CLEAN algorithm from radio astronomy (Högbom 1974). Briefly, the CLEAN procedure involves iteratively identifying the highest peak in the filtered map and subtracting off a model for the source shape centered on that peak until no peaks are left above the detection threshold. To account for several non-idealities, including finite-sized map pixels, slightly imperfect source shape models, and possibly extended sources, the source model subtraction is performed with a multiplicative factor less than unity, usually called the loop gain (after the analogous parameter in electronic feedback circuits). We use a loop gain of 0.1 in this work.

In interferometric radio observations, the source shape template in the CLEAN process is the interferometer’s “dirty beam”; in our case, it is the source shape in the filtered maps:

$$\tau' = \psi \tau. \quad (2)$$

As discussed in the previous section, the matched filter  $\psi$  was independently calculated for nine different regions of each band’s map in order to account for the map-position-dependent shape of the noise and filtering. In constructing the source shape template  $\psi\tau$ , we used the appropriate version of  $\psi$  depending on the position of the peak being CLEANed. For each source peak, we independently calculated a pre-matched-filter source shape  $\tau$  to account for this positional dependence. In the map pixelization used, this calculation consists of a simple rotation of a fiducial source shape, so this step was not unduly computationally intensive.

We ran our version of CLEAN on each band’s filtered map individually until there were no peaks above  $3\sigma$  left in the map. All map pixels identified above the  $3\sigma$  threshold were then sorted by significance and gathered into discrete sources using an association radius between  $30''$  and  $2'$ , depending on the brightness of the source. In other words, the brightest pixel found by CLEAN was declared to be the first source, then the list of pixels was examined in descending order of brightness, asking if each pixel should be declared a new source or associated with a source already identified. Source fluxes were assigned by converting the value in the filtered map of the brightest pixel associated with a source from CMB fluctuation temperature units to flux (in units of Jy) using the following relation:

$$S[\text{Jy}] = T_{\text{peak}} \times \Delta\Omega_f \times 10^{26} \times \frac{2k_B}{c^2} \left( \frac{k_B T_{\text{CMB}}}{h} \right)^2 \frac{x^4 e^x}{(e^x - 1)^2}, \quad (3)$$

where  $x = hv/(k_B T_{\text{CMB}})$  and  $\Delta\Omega_f$  is defined by

$$\Delta\Omega_f = \left[ \int dudv \psi(u, v) \tau(u, v) \right]^{-1}, \quad (4)$$

which can be thought of as the effective solid angle under the filtered source template, in that a point source of flux  $S$  will have peak brightness  $S/\Delta\Omega_f$  in the filtered map. This flux estimate will be biased for extended sources, which are discussed in Section 3.5. Source positions were obtained by calculating the center of brightness of all pixels (each pixel being  $0.25 \times 0.25$ ) associated with a given source.

<sup>27</sup> We chose this pixelization because it minimizes beam distortions, which are significant in flat-sky pixelizations in which pixel rows are at constant decl.

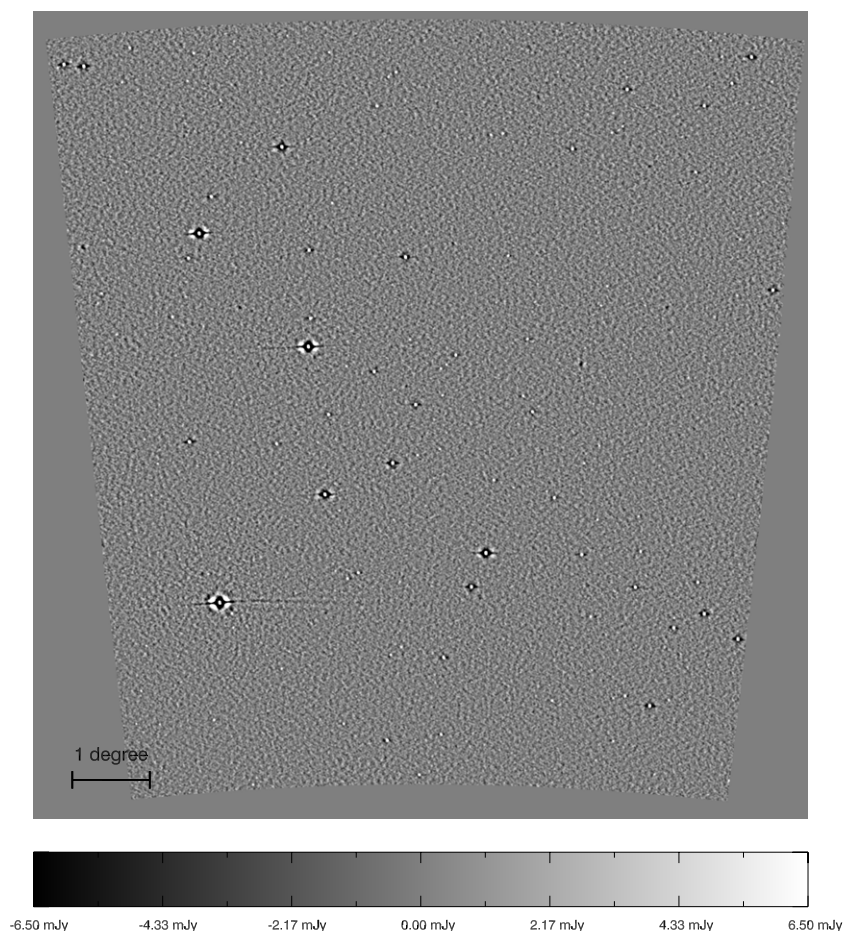


**Figure 1.** Filtered 2.0 mm map in a flat sky projection. The total sky area is  $87 \text{ deg}^2$  and the field center is R.A.  $5^{\text{h}}30^{\text{m}}$ , decl.  $-55^\circ$  (J2000). The map is oriented such that north (increasing decl.) is up and east (increasing R.A.) is left. Each pixel is  $0'.25 \times 0'.25$ . The rms in the map is 1.3 mJy, and the gray scale is  $\pm 5\sigma$ ; the brightest source is  $>500\sigma$  ( $>650 \text{ mJy}$ ), and the scale saturates for most of the sources visible here. Because of time domain filtering, the source signal produces an arc from the impulse response of the filter as the detectors scan left and right across the field. The azimuthally symmetric ringing around bright sources is due to spatial high-pass filtering in the point-source matched filter.

### 3. MAPS AND CATALOG

The filtered 2.0 mm and 1.4 mm maps used for source candidate identification are shown in Figures 1 and 2. The total area shown in each map is  $87 \text{ deg}^2$ . As previously noted, the noise varies at the level of  $\pm 5\%$  across the maps, mainly as a function of decl. This trend with decl. is due to the fact that the coverage is nearly uniform in R.A., resulting in coverage per unit solid angle that varies as  $\cos(\text{decl.})$  (i.e., the noise is systematically 5% lower at decl. =  $-60$  than at decl. =  $-55$ ). The typical rms of the map is 1.3 mJy at 2.0 mm and 3.4 mJy at 1.4 mm. The noise distribution closely approximates a Gaussian, as is evident from the central part of the pixel distributions shown in Figure 3. The fact that the maps are so uniform and the noise is so well understood makes the analysis much easier and gives us confidence in the robustness of our results.

Detections in both bands are listed in the final catalog as a single source if they are offset  $<30''$  between bands. For sources detected in both bands, we adopt the position of the more significant detection. We are far enough above the confusion limit that this simple and intuitive method is adequate. For sources detected in only one band we use the flux in the cleaned map for the second band at the position of the detection. Table 5 lists the properties of every source candidate detected above  $4.5\sigma$  in either the 2.0 mm or 1.4 mm band, while the full table listing all 3496 sources above  $3\sigma$  in either map is available in

machine-readable form in the electronic version of this paper; the full list is also available from the public SPT Web site.<sup>28</sup>

#### 3.1. Catalog Field Descriptions

Each column in Table 5 corresponds to a field in the  $87 \text{ deg}^2$  SPT two-band source catalog. Descriptions of the catalog fields/table columns are as follows:

1. Source ID: the IAU designation for the SPT-detected source.
2. R.A.: right ascension (J2000) in degrees.
3. Decl.: declination (J2000) in degrees.
4. S/N (2.0 mm): detection significance (S/N) in the 2.0 mm band.
5.  $S^{\text{raw}}$  (2.0 mm): raw flux (uncorrected for flux boosting) in the 2.0 mm band.
6.  $S^{\text{dist}}$  (2.0 mm): de-boosted flux values encompassing 16%, 50%, and 84% (68% probability enclosed, or  $1\sigma$  for the equivalent normal distribution) of the cumulative posterior probability distribution for 2.0 mm flux, as estimated using the procedure described in Section 4.
7. S/N (1.4 mm): same as (4), but for 1.4 mm.
8.  $S^{\text{raw}}$  (1.4 mm): same as (5), but for 1.4 mm.

<sup>28</sup> <http://pole.uchicago.edu/public/data/vieira09/>

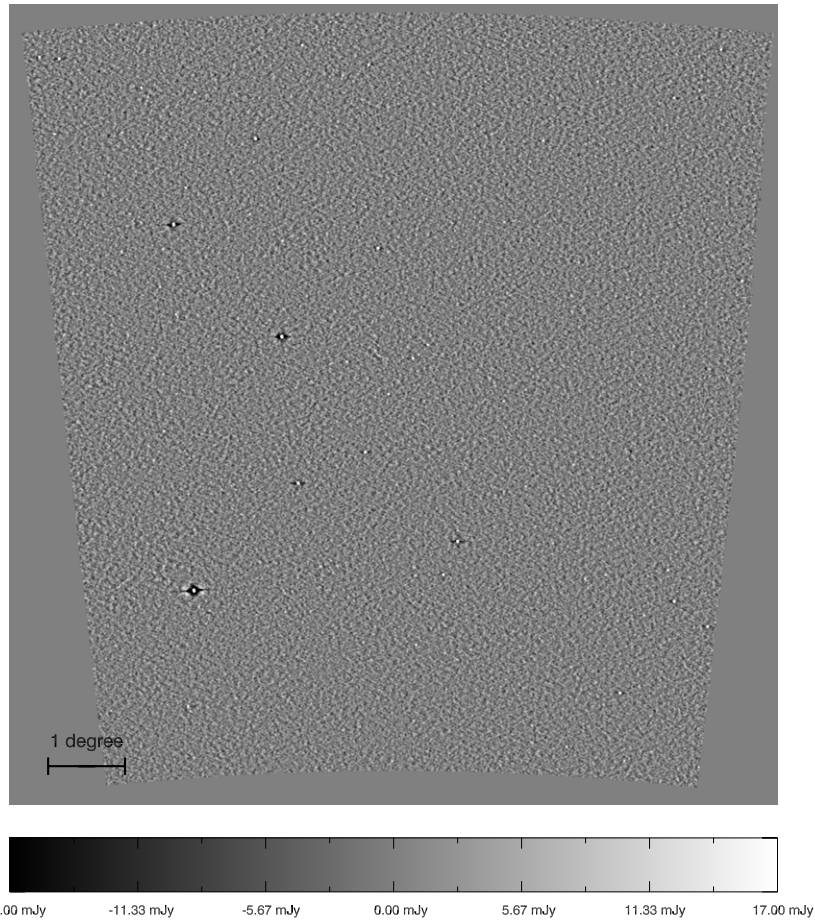


**Figure 2.** Filtered 1.4 mm map. The rms in the map is 3.4 mJy, the gray scale is  $\pm 5\sigma$ , and the brightest source is  $>150\sigma$  ( $>550$  mJy). See the corresponding Figure 1 for comments common to both maps.

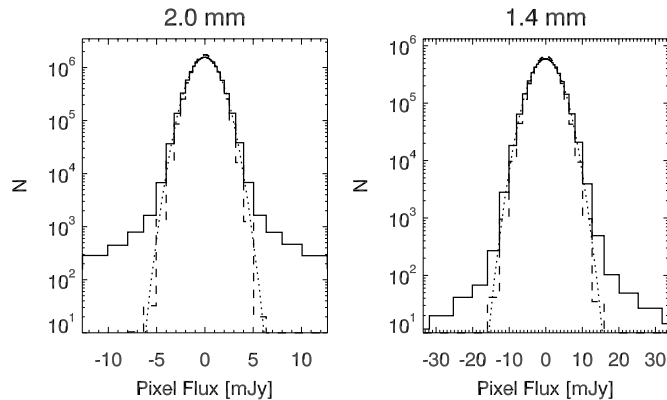


**Figure 3.** Distribution of fluxes in map pixels. For each band, the lines are as follows: solid, the co-added signal map; dashed, the co-added difference map (see Section 2.4); dotted, fit to the signal map pixel histogram noise peak. For each band, the fit is done to the full signal map and gives  $\sigma = 1.3$  mJy for 2.0 mm and  $\sigma = 3.4$  mJy for 1.4 mm. The noise across the map is Gaussian. The negative tails are mainly due to ringing from the various effective high-pass filters on the sources in the map.

9.  $S^{\text{dist}}$  (1.4 mm): same as (6), but for 1.4 mm.
10.  $\alpha^{\text{raw}}$ : estimate (from the raw flux in each band) of the 2.0 mm–1.4 mm spectral index  $\alpha$ , where  $\alpha$  is the slope of the (assumed) power-law behavior of source flux as a function of wavelength:

$$S \propto \lambda^{-\alpha}. \quad (5)$$

11.  $\alpha^{\text{dist}}$ : 16%, 50%, and 84% estimates of the spectral index, based on the probability distributions for spectral index estimated using the procedure described in Section 4.
12.  $P(\alpha > 1.66)$ : fraction of the spectral index posterior probability distribution above the threshold value of 1.66. A higher value of  $P$  means the source is more likely to be dust-dominated.
13. Type: source classification (synchrotron- or dust-dominated), based on whether  $P(\alpha > 1.66)$  is greater than or less than 0.5.
14. Nearest SUMSS source: angular distance (in arcseconds) from the nearest source in the 36 cm (843 MHz) Sydney University Molongolo Sky Survey (SUMSS; Mauch et al. 2003). There are 2731 SUMSS sources in the SPT survey area. For a  $1'$  association radius there is a 2.7% chance of random association for each SPT source.
15. Nearest RASS source: angular distance (in arcseconds) from the nearest source in the *ROSAT* All-Sky Survey (RASS) Bright Source Catalog (Voges et al. 1999) or Faint Source Catalog (Voges et al. 2000). There are 1441 RASS sources in the SPT survey area. For a  $1'$  association radius there is a 1.4% chance of random association for each SPT source.
16. Nearest *IRAS* source: angular distance (in arcseconds) from the nearest source in the *IRAS* Faint-Source Catalog (*IRAS-FSC*; Moshir et al. 1992). There are 493 *IRAS* sources in the SPT survey area. For a  $1'$  association radius there is a 0.8% chance of random association for each SPT source.

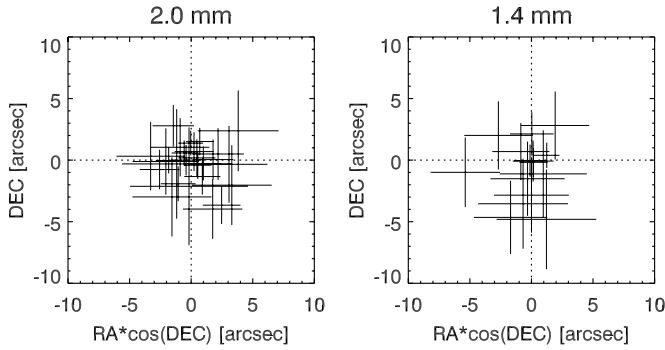


**Figure 4.** Comparison of relative pointing offsets between the SPT bands and AT20G catalog sources. Only sources with  $S/N > 10$  which have a robust counterpart within  $20''$  have been plotted. The errors for the SPT positions were estimated following Ivison et al. (2007). The errors plotted here are a quadrature sum of the SPT error and the quoted error from the AT20G catalog. The rms for both SPT bands is  $< 3''$ .

### 3.2. Astrometry

SPT pointing is reconstructed through a combination of an online pointing model (tied to regular observations with optical star cameras), corrections based on observations of galactic H II regions (performed many times each observing day), and information from thermal and linear displacement sensors on the telescope. The pointing reconstruction process is described in more detail in S09 and Carlstrom et al. (2009). In this work, we calibrate the absolute positions in the maps by comparing our best-fit positions for bright sources ( $S/N > 10$ ) in our catalog with external determinations of those positions from the 1.5 cm Australia Telescope 20 GHz Survey (AT20G) catalog, in which the absolute astrometry is tied to very long baseline interferometry calibrators and is accurate at the  $1''$  level (Murphy et al. 2010). We used 15 point sources for the 1.4 mm absolute astrometry correction and 26 point sources for 2.0 mm. Figure 4 shows the distribution of offsets between SPT-determined positions and AT20G positions.

### 3.3. Completeness and Purity

#### 3.3.1. Completeness

We follow Scott et al. (2008) and estimate our completeness by placing simulated sources in the actual signal maps and performing the source extraction as with the real data. For the simulated source profile, we use the measured beam convolved

with the map-domain estimate of our timestream filtering and the matched filter. As with the matched filter and the CLEAN process, we use a different simulated source profile in each of the nine map tiles (see Section 2.4 for details). The simulated source is considered to be detected if it would have made it into our catalog—i.e., if it is detected by the source extraction algorithm at  $\geq 3\sigma$ . As expected for maps whose variance is nearly uniform and is dominated by random, Gaussian-distributed noise, our cumulative completeness curves (fraction of simulated sources detected above a given flux) are fit well by error functions, as shown in Figure 5. The exact functional form used here is

$$f_{\text{compl}}(S) = \frac{1}{\sqrt{2\pi\sigma^2}} \int_S^\infty e^{-(S'-S_0)^2/2\sigma^2} dS'. \quad (6)$$

On the basis of this test and the error-function fits, we expect the full  $\geq 3\sigma$  catalog to be 50% complete at 3.5 and 9.1 mJy in the 2.0 and 1.4 mm bands and to be 95% complete at 5.5 mJy and 14.1 mJy in the 2.0 and 1.4 mm bands.

#### 3.3.2. Purity

There is some ambiguity in the definition of “purity” or “false detection” when one is dealing with a source population with steep differential number counts, especially if the detected fluxes are anywhere near the confusion limit. In such a situation, there will be at least one source at a non-negligible fraction of the detection threshold in every beam. In this work, we have chosen to define a false detection as a fluctuation above the detection threshold in the absence of any mean point source contribution to the maps. We treat the problem of low-flux sources scattering above the detection threshold in the context of flux boosting in Section 4.

We estimate our purity using two different methods, both of which are fairly common in the SMG literature (e.g., Perera et al. 2008). First, we invert our maps and run the matched filter and source-finding algorithm on the negative maps. This method is complicated by the fact that, at 2.0 mm, we expect to have a real negative signal near the beam scale due to the thermal SZ signal from galaxy clusters. To deal with this, we mask the inverted 2.0 mm map around SZ cluster candidates detected at  $\geq 4.5\sigma$ . These candidates are identified using a filter optimized for extended sources with a particular spatial profile (in this case a spherical  $\beta$  model; see S09 for details), so we should not be masking point-like noise fluctuations with this procedure. Our second estimate of purity comes from running the matched

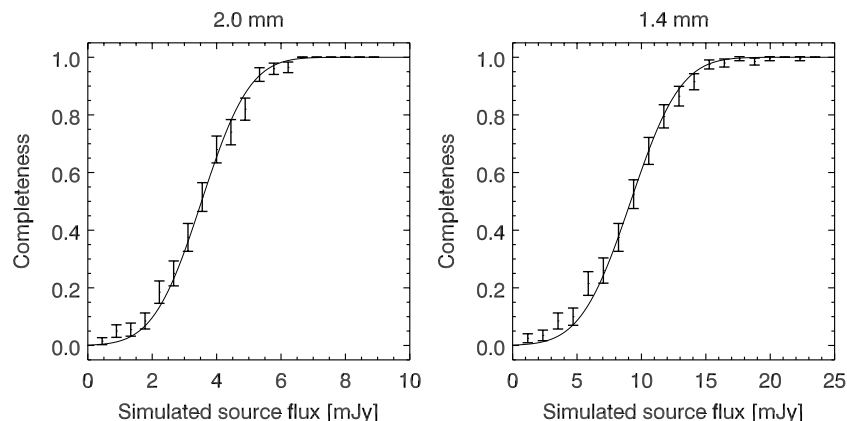


**Figure 5.** Left panel shows the results of the completeness simulation at 2.0 mm and right panel shows the results of the completeness simulation at 1.4 mm. In each plot, the symbols with error bars show the fraction of sources recovered at  $> 3\sigma$  with error bars estimated from binomial statistics. The dashed line shows the best-fit model of the form shown in Equation (6).

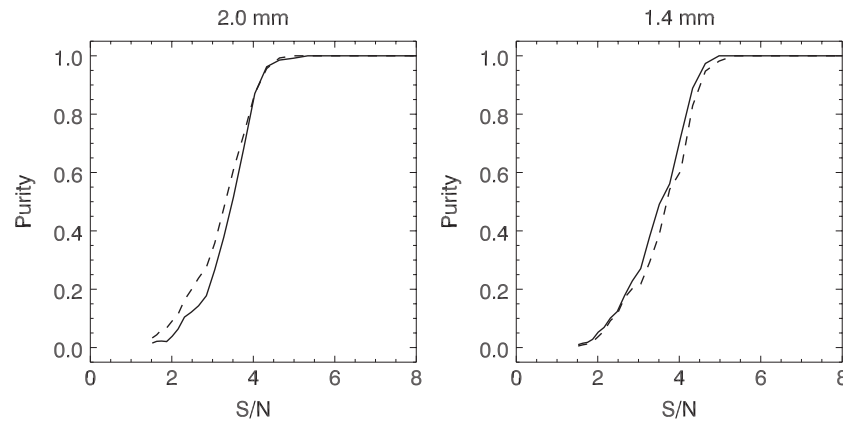


**Figure 6.** Purity in the 2.0 mm selected sample (left) and the 1.4 mm selected sample (right). In each plot, the solid line indicates the purity (see Equation (7)) calculated using the inverted map to estimate the number of false detections, while the dashed line indicates the purity calculated using simulated maps to estimate the number of false detections. The situation is more complicated at 2.0 mm than at 1.4 mm due to the presence of SZ (see Section 3.3.2 for details).

filter and source-finding algorithm on simulated maps. These simulated maps contain atmospheric and instrumental noise (taken from our difference map; see Section 2.4), a realization of the CMB, and a white, Gaussian noise term meant to approximate the contribution from the background of sources below the detection threshold. The results from both tests are shown in Figure 6. In all cases, the quantity plotted is

$$f_{\text{pure}} = 1 - \frac{N_{\text{false}}}{N_{\text{total}}}, \quad (7)$$

where  $N_{\text{false}}$  is the number of false detections (as estimated, alternately, by one of the two methods described above) above a given S/N and  $N_{\text{total}}$  is the total number of detections above a given S/N in the real map. Both methods agree that at  $S/N > 4.5$  our sample is  $\gtrsim 90\%$  pure. Perera et al. (2008) argue that both methods will overestimate the true false detection rate, and this hypothesis is supported by the fraction of our synchrotron-dominated sources that have clear counterparts in other catalogs and/or our Australia Telescope Compact Array (ATCA) follow-up observations (see Section 6 for details).

### 3.3.3. Contamination at 2.0 mm from SZ

In addition to complicating the purity analysis in the previous section, SZ decrements from galaxy clusters have the potential to contaminate our source measurements at 2.0 mm (though not at 1.4 mm, which is very close to the thermal SZ null). We believe that this contamination will be negligible at the source flux levels considered here for two reasons. One reason is because clusters are expected to be at least partially resolved by the SPT at 2.0 mm, meaning that their contribution to maps filtered to optimize point-source sensitivity will be diminished. The other reason is that the number density of clusters with decrements deep enough to significantly affect the source fluxes presented here is expected to be quite low. The SZ contamination will be somewhat boosted by the fact that the sources we investigate here are expected to be spatially correlated with galaxy clusters at some level (e.g., Coble et al. 2007; Bai et al. 2007), but we expect the net effect to be negligible even after accounting for this correlation.

To make these arguments more quantitative, we investigate the level of flux decrements in simulated SZ maps filtered in the same way the SPT data is filtered in this work. We take simulated 2.0 mm maps created using the technique described in Shaw et al. (2009), filter them with the estimate of the SPT 2.0 mm

beam and filtering discussed in Section 2.4.1 to simulate SPT observation and data processing, and further filter them with the matched filter from Section 2.4.1. Finally, we convert the filtered map from temperature to flux (as in Section 2.4.2) and record the decrement in Jy at each simulated cluster location. We find roughly five clusters per square degree with at least a 1.3 mJy decrement in the filtered map—equivalent to a  $1\sigma$  noise fluctuation in the 2.0 mm SPT map. We find roughly one cluster per  $10 \text{ deg}^2$  with at least a 5.8 mJy decrement in the filtered map—equivalent to a  $4.5\sigma$  noise fluctuation in the 2.0 mm SPT map.

The SPT beam is roughly  $1'$  wide at 2.0 mm, meaning that there are over 1000 independent resolution elements in  $1 \text{ deg}^2$  of the SPT 2.0 mm map. Thus, if galaxy clusters were randomly distributed with respect to sources in the SPT maps, we would expect fewer than 0.5% of sources to suffer a  $1\sigma$  or worse systematic flux reduction due to cluster SZ signal, and we would expect fewer than 0.01% of  $4.5\sigma$  sources to be completely canceled by an SZ decrement. Coble et al. (2007) estimate that radio sources are a factor of  $9 \pm 4$  times more likely to be found along a line of sight within  $0.5$  of a cluster than in the field. This boosts the chance of a systematic  $1\sigma$  flux error to  $\lesssim 5\%$  and the chance of a  $4.5\sigma$  error to  $\lesssim 0.1\%$ . Dust-dominated sources are expected to be less correlated with galaxy clusters than radio sources Bai et al. (2007), so the effect will be even smaller for these sources. The effect of this level of systematic flux error on our final counts is completely subdominant to the statistical uncertainty.

### 3.4. Raw Spectral Classification and Source Association

Based on previous surveys of sources at other wavelengths, we expect most SPT sources to belong to one of two populations: one dominated by synchrotron emission, the members of which should have an emission spectrum that is flat or falling with decreasing wavelength, and one dominated by thermal emission of reprocessed starlight by dust, the members of which should have an emission spectrum that increases with decreasing wavelength. Our results confirm this picture. Of course, any individual source may have components of each in its emission and the local slope of the spectral energy distribution (SED) will be further modulated by the redshift of the source. Though our actual source characterization is based on the integrated posterior probability density function (PDF) of the spectral index, estimated using the method described in Section 4.2, a

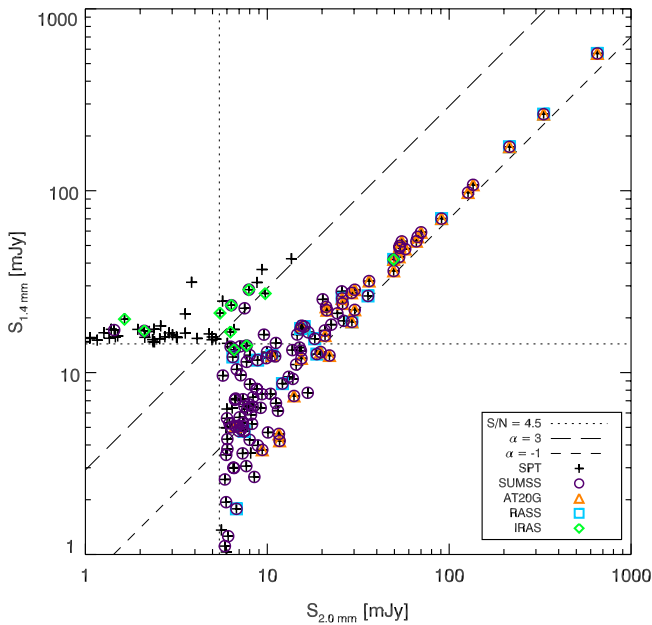


**Figure 7.** Raw 1.4 mm flux vs. raw 2.0 mm flux for sources detected above  $4.5\sigma$  (dotted lines) in either band. Long-dashed line: a spectral index  $\alpha = 3$  typical for sources dominated by dust emission. Short-dashed line: a spectral index  $\alpha = -1$  typical for sources dominated by synchrotron emission. By finding associations within  $1'$  for SUMSS (purple circles), AT20G (orange triangles), RASS (light blue squares), and *IRAS* (green diamonds), we see that most synchrotron-dominated sources are previously known. The bright dust-dominated population without counterparts in *IRAS* is discussed in Section 7.2.

plot of raw 1.4 mm flux versus raw 2.0 mm flux, as in Figure 7, gives the basic picture. Of the sources detected above  $4.5\sigma$  in both bands, the synchrotron-dominated sources occupy a locus of points close to the line  $\alpha = -1$ , where the spectral index  $\alpha$  is defined in Equation (5). The dust-dominated sources detected in both bands occupy a clearly separated locus of points close to the  $\alpha = 3$  line. Also worth noting in this plot is that effectively all of the high-S/N synchrotron-dominated sources have counterparts in external catalogs, while many of the high-S/N dust-dominated sources do not. This point is explored in more detail in Sections 6 and 7.2.

### 3.5. Extended Sources and Other Notes

As is evident from Equations (3) and (4), our flux estimates rest on the assumption that all sources have the same shape in our filtered maps. Since the assumed source shape is just that of our beam and filtering, this assumption will only be valid for point-like objects. This method will not provide accurate flux estimates for resolved sources. For example, our method will underestimate the flux of a source with an FWHM =  $0'.25$  Gaussian profile by 3% at 2.0 mm and 4% at 1.4 mm; a  $0'.5$  source will be underestimated by 10% and 11%; a  $1'$  source by 31% and 36%.

Given the  $\sim 1'$  beam of the SPT, we expect that few emissive sources will appear extended in our maps. With  $1'$  resolution, a normal galaxy will appear point-like at redshifts  $z \gtrsim 0.05$  (distances greater than  $\sim 200$  Mpc), so only very nearby objects or objects with very extended structure (such as AGNs with 100 kpc scale jets) would appear extended in our maps. Furthermore, the matched filter applied to the maps is optimized for unresolved sources and will degrade the S/N on any extended source.

We search for extended sources by fitting a cut-out of the (unfiltered) map around each detected source to a model of our

measured beam convolved with a Gaussian of variable width. We then identify sources for which the best-fit FWHM is at least  $0'.25$  and is inconsistent with zero at the  $3\sigma$  level. We also visually inspect the filtered map at each  $\geq 4.5\sigma$  source location for possible extended sources and any other anomalies.

Of the 188 sources detected with  $S/N \geq 4.5$  in either band, 11 have a best-fit width of at least  $0'.25$  and are inconsistent with zero width at  $\geq 3\sigma$ . These sources are noted in Table 5 with an “a” next to the source name. Of these 11 sources, nine fall into our synchrotron-dominated class and have counterparts in the SUMSS or Parkes–MIT–NRAO (PMN; Wright et al. 1994) catalogs. Three of these nine sources are also listed in the SUMSS catalog as having detectable extent beyond the  $\sim 30''$  SUMSS beam. The remaining two sources that we identify as extended are nearby IR-luminous galaxies that are also detected with *IRAS*. Our visual inspection of all sources above  $4.5\sigma$  in either band revealed the following cases of note (some of which are also identified by the quantitative test for extended structure).

SPT-S J051614–5429.6: this detection may be spurious, caused by sidelobes from the deep SZ decrement at 2.0 mm from the galaxy cluster SPT-CL J0516–5430 (also RXCJ0516.6–5430 and Abell S0520). There is no counterpart at 1.4 mm or in external catalogs, the source is classified as extended by the method described above, and visual inspection shows it to have an irregular shape. The other bright source very near to a galaxy cluster with a deep SZ decrement, SPT-S J050907–5339.2 (near SPT-CL J0509–342) is almost certainly not spurious, since it is detected more strongly at 1.4 mm (which is near the SZ null) than at 2.0 mm. Evidence of this source is also seen in data taken with the Atacama Cosmology Telescope (Hincks et al. 2010).

SPT-S J051217–5724.0: this source is classified as extended, and visual inspection reveals a clear offset between the 2.0 mm and 1.4 mm emission. The emission in both bands is almost certainly associated with the low-redshift ( $z = 0.0047$ ) galaxy NGC 1853; we appear to be resolving different components of emission within the galaxy. We see a similar configuration in SPT-S J050656–5943.2, which is associated with the  $z = 0.0041$  galaxy NGC 1824, and SPT-S J055116–5334.4, which is associated with the  $z = 0.015$  galaxy ESO 160-G 002. We also see offsets between 1.4 mm and 2.0 mm emission in SPT-S J051116–5341.9 which has no obvious counterparts in existing catalogs.

SPT-S J052850–5300.3: we classify this source as dust-dominated and it has no counterpart in the *IRAS*-FSC. There is a SUMSS source  $45''$  away, and visual inspection reveals a low-significance 2.0 mm counterpart exactly coinciding with the SUMSS location. The 1.4 mm emission, however, is clearly offset from both the 2.0 mm emission and the SUMSS location, indicating that this may be a chance superposition of a known radio source and a previously unknown dust-dominated source.

## 4. CORRECTING FOR FLUX BOOSTING AND ESTIMATING SPECTRAL BEHAVIOR

The differential counts of mm-wave selected point sources as a function of source flux are expected to be very steep, so the measured flux of a point source in the SPT survey will almost certainly suffer flux boosting. In this work, we define flux boosting as the increased probability that a source we measure to have flux  $S$  is really a dimmer source plus a positive noise fluctuation relative to the probability that it is a brighter source plus a negative noise fluctuation. Because of this asymmetric probability distribution, raw measurements of source flux will

be biased high.<sup>29</sup> The standard method in the SMG literature for dealing with this problem (e.g., Coppin et al. 2005) is to construct a posterior probability distribution for the intrinsic flux of each detection. The situation with SPT data is more complicated for two reasons. (1) As discussed in Crawford et al. (2010), the current implementation of this method in the SMG literature is not appropriate for estimating properties of individual sources, which is a key aim of this work. (2) We have data in more than one observing band, and the prior information that is applied to create the posterior flux likelihood will be highly correlated in the two bands.

In Crawford et al. (2010), we develop a method of correcting for flux boosting (based on the Bayesian posterior method used in Coppin et al. 2005 and others) which preserves information on individual source properties, and we extend that method to estimate the intrinsic multi-band flux of a source based on the measured flux in each band and the prior knowledge of the source populations in the various bands. In the two-band SPT case, the final product for each source is a two-dimensional posterior likelihood, where the two variables are either the flux in each band or the flux in one band and the spectral index between bands. The two likelihood distributions are trivially related by

$$\begin{aligned} P(S_{\max,1}, S_{\max,2} | S_{p,m,1}, S_{p,m,2}) \\ = P(S_{\max,1}, \alpha | S_{p,m,1}, S_{p,m,2}) \frac{d\alpha}{dS_{\max,2}}, \end{aligned} \quad (8)$$

where  $S_{p,m,i}$  is the measured flux in a resolution element or pixel in band  $i$ ,  $S_{\max,i}$  is the true flux of the brightest source in that resolution element and band, and  $d\alpha/dS_{\max,2}$  is derived from Equation (5). If we cast our prior information on source behavior in terms of source counts in one band and spectral behavior between bands, and we make the assumption that spectral index does not depend on flux, then we can write

$$\begin{aligned} P(S_{\max,1}, \alpha | S_{p,m,1}, S_{p,m,2}) \\ \propto P(S_{p,m,1}, S_{p,m,2} | S_{\max,1}, \alpha) P(S_{\max,1}) P(\alpha) \end{aligned} \quad (9)$$

(see Crawford et al. 2010 for details). Of course, we expect that the spectral index distribution of our sources will in fact depend on flux. But the prior that we choose to place on  $\alpha$  (see Section 4.1) is broad enough that it easily encompasses the full expected spectral index distribution at all fluxes.

The posterior probability distributions in Equations (8) and (9) are used to calculate most of the quantities reported in subsequent sections, including the 16%, 50%, and 84% (68% probability enclosed about the median) percentiles for de-boosted flux listed in Table 5; the probability distributions for 2.0–1.4 mm spectral index, from which the 16%, 50%, and 84% percentiles for that quantity in Table 5 are derived; and the source counts shown in Figures 9, 10, and 12.

#### 4.1. Choice of Priors

To construct the prior  $P(S_{\max,1})$  in Equation (9), we need assumptions for the source counts as a function of flux ( $dN/dS$ )

<sup>29</sup> This phenomenon is closely related to what is referred to in the literature as “Eddington bias” (e.g., Teerikorpi 2004); however, the consensus use of the term in the literature is to describe the bias introduced to estimation of source counts versus brightness, not on the estimated brightness of individual sources. This usage is consistent with the original work of Eddington (1913). As such, we choose to use “flux boosting” for the effect on individual source flux estimation.

in each of our bands. We assume the counts in each band will be the sum of dust-dominated and synchrotron-dominated counts, and we use estimates of counts for each of these populations from the literature, extrapolated to our wavelength bands when necessary. For the dust-dominated population, we use the Negrello et al. (2007) model for counts at 850  $\mu\text{m}$ , extrapolated to our wavelengths using a spectral index of 3.0 for the SMGs and 2.0 for the *IRAS*-type galaxies (assuming zero scatter in the index in both cases). The choice of these spectral indices was taken from an Arp220 SED template and the outcome is not very sensitive to the input.<sup>30</sup> De Zotti et al. (2005) make direct predictions for the synchrotron-dominated population counts at 2.0 mm, which we use without modification. We extrapolate these predictions to 1.4 mm using a Gaussian distribution of spectral indices, centered on  $-0.5$  with rms of 0.5. We have found that the choice of source-count prior makes only a small difference in the resulting posterior probability distributions (in the S/N range presented in this paper), consistent with the result in Scott et al. (2008). Section 2.6 of the companion paper (Crawford et al. 2010) describes the interplay of experimental and prior information.

For the spectral index prior, we have chosen a flat prior between  $\alpha = -3$  and  $\alpha = 5$ . Given what is known about the two populations that are expected to contribute to sources at our wavelengths (e.g., Knox et al. 2004; Mason et al. 2009), this estimate conservatively brackets the expected spectral behavior of SPT sources. (The difference in derived counts by choosing a flat prior from  $\alpha = -2$  to  $\alpha = 4$  is negligible.) Section 3.1 of the companion paper, Crawford et al. (2010), describes a subtlety of choosing the counts prior in parallel with a prior on the spectral index because the two are interdependent. In this work, we use a 1.4 mm counts model prior for the derived 1.4 mm counts and a 2.0 mm counts model prior for the derived 2.0 mm counts. This means that in the derived 1.4 mm counts, information that comes from the 2.0 mm band is translated to 1.4 mm flux using the flat prior from  $\alpha = -3$  to  $\alpha = 5$  (and similarly for the cross-band information for the 2.0 mm counts).

#### 4.2. Spectral Index Estimation and Source Classification Method

By marginalizing the two-dimensional posterior in Equation (9) over the flux in the detection band  $P(S_{\max,1})$ , we obtain a posterior likelihood for the spectral index of each detected source. The 16%, 50%, and 84% values of  $\alpha$  given in Table 5 are taken from the cumulative version of this likelihood distribution for each source. These individual distributions can be summed to produce the measured  $\alpha$  distribution of all sources detected in our two bands (which will be the convolution of the intrinsic distribution with a complicated function of the noise from instrumental, atmospheric, and source background contributions in both bands). Figure 8 shows that the posterior spectral index distribution for sources at S/N > 4.5 in both bands has a clear population split. We use this split to identify the sources as either dust or synchrotron dominated through the posterior.

In Table 5, a source with  $P(\alpha > 1.66) > 0.5$  (having >50% of its posterior index distribution in excess of 1.66) is classified as dust dominated and a source with  $P(\alpha > 1.66) < 0.5$  (having <50% of its posterior index distribution in excess of 1.66) is classified as synchrotron dominated. The source counts

<sup>30</sup> While we compare to the integral counts predictions of Lagache et al. (2004) in Section 7.2, we found that a kink in those differential counts produced a bias toward drawing  $\sim 10$  mJy sources from the posterior. Negrello et al. (2007) was then used by virtue of its smoothness.

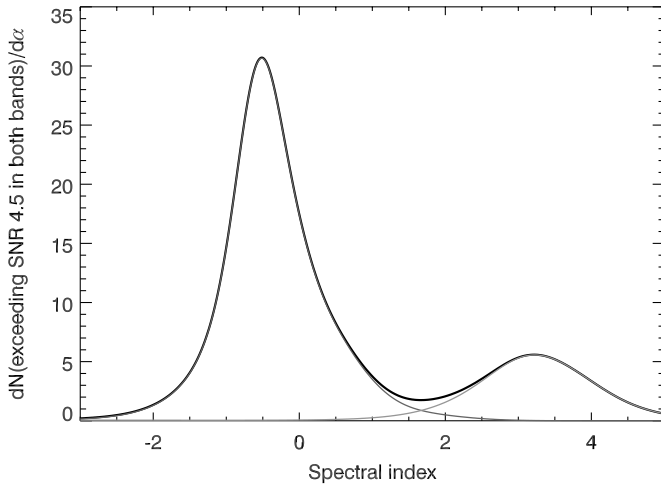


**Figure 8.** Distribution of the posterior spectral indices measured between 1.4 mm and 2.0 mm for sources with  $S/N > 4.5$  in both bands (thick black line). Because we take a flat prior on the spectral index between  $-3$  and  $5$  (and zero outside), the distribution outside the plotted range here goes to zero. We sum the  $P(\alpha)$  for each source (described in Section 4.2 and normalize it such that the integral over  $\alpha$  is equal to 1 for each source) to give an effective  $dN/d\alpha$  for this selection. We then classify the source by the probability that its posterior spectral index distribution exceeds a classification cut, taken here to be  $\alpha = 1.66$ . (This threshold is at the minimum of  $dN/d\alpha$  between the two populations.) Sources with  $>50\%$  probability of posterior  $\alpha > 1.66$  are classified as dust dominated and those with  $<50\%$  probability of posterior  $\alpha > 1.66$  are synchrotron dominated. There are 11 dust sources (light gray) and 41 synchrotron sources (dark gray) that contribute to this distribution. The population split shown here is robust to changes in the  $S/N$  cut. At lower  $S/N$  cuts, the population features broaden slightly and many sources have poorly localized  $P(\alpha)$  distributions which contribute a floor in  $dN/d\alpha$ .

by population use a probabilistic method based on  $P(\alpha)$  that is described in Section 5, but there, too, we take  $\alpha = 1.66$  to be the threshold. This value of the threshold is the spectral index at the minimum of  $dN/d\alpha$  between the two populations (see Figure 8). The source counts presented here are insensitive (within their uncertainty) to this choice of threshold over the range  $\alpha = (1.66 \pm 0.5)$ ; this particular value is chosen for definiteness.

## 5. SINGLE-BAND SOURCE COUNTS

Using the flux measurements in each band, we estimate the probability distribution of intrinsic fluxes for each source by constructing the two-band posterior likelihood  $P(S_{\max,1}, S_{\max,2} | S_{p,m,1}, S_{p,m,2})$  as described in Section 4. To derive the counts as a function of flux from these distributions of intrinsic fluxes, we apply a bootstrap method similar to the one described in Austermann et al. (2010). Here, for each source, we randomly draw  $5 \times 10^4$  intrinsic fluxes from the two-band posterior, forming effectively  $5 \times 10^4$  mock catalogs of intrinsic fluxes in both bands. For each catalog, we draw a subset of these sources with replacement, where the number of sources drawn is a Poisson-deviate of the catalog size. This resampling accounts for sample variance but not cosmological variance (which would require an additional variance term to describe how counts are expected to vary from sky patch to sky patch because of large-scale structure).

For each of these  $5 \times 10^4$  resampled catalogs, we estimate  $dN/dS$  and  $N(>S)$ . In each flux bin, we then find the 16%, 50%, and 84% percentile points (that is, 68% of the enclosed probability around the median) of the distributions of  $dN/dS$  and  $N(>S)$  in that bin. This yields the equivalent of  $1\sigma$

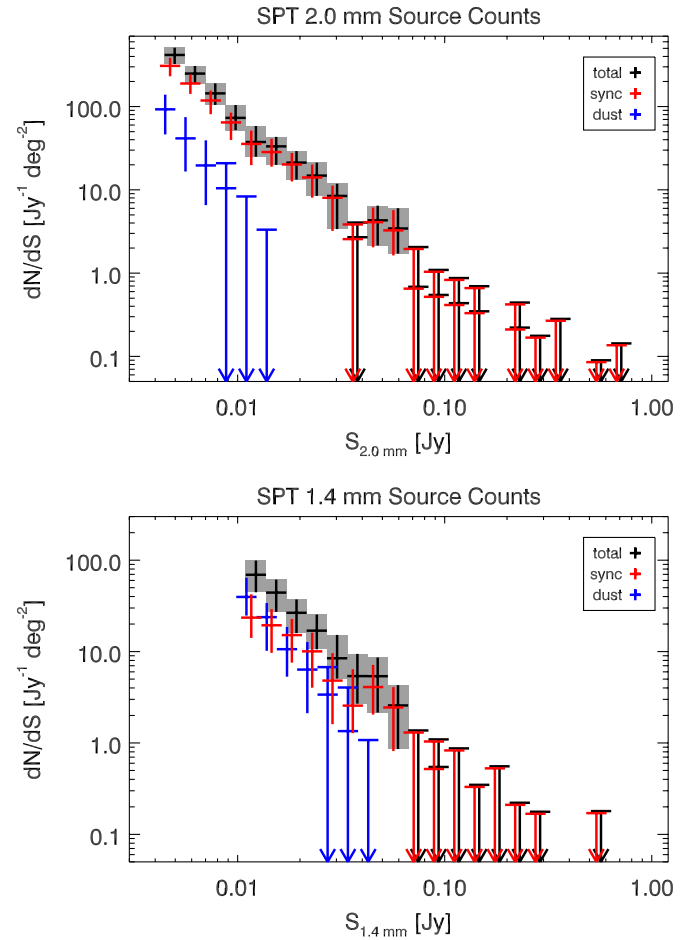


**Figure 9.** Differential source counts by population for the 2.0 mm (upper plot) and 1.4 mm (lower plot) bands. Gray boxes and black crosshairs indicate the total counts in that band. Red crosshairs indicate the synchrotron-dominated population counts and blue crosshairs indicate the dust-dominated counts. Crosshairs with full error enclose 68% of the probability about the median and are estimated in the bootstrap over flux described in Section 5. Here we have offset the two populations slightly in flux so that they do not lie on top of one another and the total counts are at zero offset. A source is identified as synchrotron dominated (dust dominated) if  $\alpha < 1.66$  ( $\alpha \geq 1.66$ ) in the bootstrap resampling from the joint posterior flux distributions, see Section 5. This splits the populations so that their differential counts sum to the total counts. A correction for survey completeness from simulations described in Section 3.3 is also applied and impacts primarily the 1.4 mm counts in the lowest two flux bins.

normally distributed errors in each flux bin. The  $N(>S)$  and  $dN/dS$  bootstraps account for sample variance and posterior distribution variance (which includes noise, calibration error, deboosting, and cross-band information). Because the posterior flux distributions per source span several flux bins in the counts, even the errors on differential counts will be correlated. The counts are corrected for the completeness using the simulations described in Section 3.3.1. Figure 9 shows differential counts in both bands as well as the differential counts of populations that we identify as either dust or synchrotron dominated. The counts are given in numerical form in Tables 1–4.

The discrimination into synchrotron and dust-dominated counts is included in the bootstrap method. Here, each catalog resampling will have drawn intrinsic fluxes at 1.4 mm and 2.0 mm, and so each source in that catalog will have a spectral index. The dust-dominated (synchrotron-dominated) counts are derived from those sources that have  $\alpha > 1.66$  ( $\alpha < 1.66$ ) in the resampling. A source with  $P(\alpha > 1.66) > 0.3$  will therefore

**Table 1**  
2.0 mm Differential Counts

Flux Range (Jy)	$dN/dS$ Total ( $\text{Jy}^{-1} \text{ deg}^{-2}$ )	$dN/dS$ Sync ( $\text{Jy}^{-1} \text{ deg}^{-2}$ )	$dN/dS$ Dust ( $\text{Jy}^{-1} \text{ deg}^{-2}$ )	Completeness
$4.4 \times 10^{-3}$ – $5.6 \times 10^{-3}$	$(4.17^{+0.9}_{-0.9}) \times 10^2$	$(3.24^{+0.8}_{-0.8}) \times 10^2$	$(9.26^{+4.6}_{-4.6}) \times 10^1$	0.88
$5.6 \times 10^{-3}$ – $7.0 \times 10^{-3}$	$(2.49^{+0.6}_{-0.6}) \times 10^2$	$(1.99^{+0.6}_{-0.5}) \times 10^2$	$(4.15^{+3.3}_{-2.5}) \times 10^1$	0.98
$7.0 \times 10^{-3}$ – $8.7 \times 10^{-3}$	$(1.44^{+0.5}_{-0.4}) \times 10^2$	$(1.24^{+0.4}_{-0.4}) \times 10^2$	$(1.96^{+2.0}_{-1.3}) \times 10^1$	1.00
$8.7 \times 10^{-3}$ – $1.1 \times 10^{-2}$	$(7.32^{+3.1}_{-2.1}) \times 10^1$	$(6.79^{+2.1}_{-2.6}) \times 10^1$	$(1.05^{+1.0}_{-1.0}) \times 10^1$	1.00
$1.1 \times 10^{-2}$ – $1.4 \times 10^{-2}$	$(3.75^{+2.1}_{-1.3}) \times 10^1$	$(3.75^{+1.7}_{-1.7}) \times 10^1$	$0^{+8.3}_{-0}$	1.00
$1.4 \times 10^{-2}$ – $1.7 \times 10^{-2}$	$(3.33^{+1.0}_{-1.3}) \times 10^1$	$(2.99^{+1.3}_{-1.0}) \times 10^1$	$0^{+3.3}_{-0}$	1.00
$1.7 \times 10^{-2}$ – $2.2 \times 10^{-2}$	$(2.12^{+0.8}_{-0.8}) \times 10^1$	$(2.12^{+0.8}_{-0.8}) \times 10^1$		1.00
$2.2 \times 10^{-2}$ – $2.7 \times 10^{-2}$	$(1.48^{+0.6}_{-0.6}) \times 10^1$	$(1.48^{+0.6}_{-0.6}) \times 10^1$		1.00
$2.7 \times 10^{-2}$ – $3.4 \times 10^{-2}$	$8.45^{+3.4}_{-5.1}$	$8.45^{+3.4}_{-5.1}$		1.00
$3.4 \times 10^{-2}$ – $4.2 \times 10^{-2}$	$2.70^{+1.3}_{-2.7}$	$2.70^{+1.3}_{-2.7}$		1.00
$4.2 \times 10^{-2}$ – $5.3 \times 10^{-2}$	$4.30^{+2.2}_{-2.2}$	$4.30^{+2.2}_{-2.2}$		1.00
$5.3 \times 10^{-2}$ – $6.7 \times 10^{-2}$	$3.43^{+2.6}_{-1.7}$	$3.43^{+2.6}_{-1.7}$		1.00
$6.7 \times 10^{-2}$ – $8.3 \times 10^{-2}$	$(6.85^{+13.7}_{-6.9}) \times 10^{-1}$	$(6.85^{+13.7}_{-6.9}) \times 10^{-1}$		1.00
$8.3 \times 10^{-2}$ – $1.0 \times 10^{-1}$	$(5.47^{+5.5}_{-5.5}) \times 10^{-1}$	$(5.47^{+5.5}_{-5.5}) \times 10^{-1}$		1.00
$1.0 \times 10^{-1}$ – $1.3 \times 10^{-1}$	$(4.36^{+4.4}_{-4.4}) \times 10^{-1}$	$(4.36^{+4.4}_{-4.4}) \times 10^{-1}$		1.00
$1.3 \times 10^{-1}$ – $1.6 \times 10^{-1}$	$(3.48^{+3.5}_{-3.5}) \times 10^{-1}$	$(3.48^{+3.5}_{-3.5}) \times 10^{-1}$		1.00
$2.1 \times 10^{-1}$ – $2.6 \times 10^{-1}$	$(2.22^{+2.2}_{-2.2}) \times 10^{-1}$	$(2.22^{+2.2}_{-2.2}) \times 10^{-1}$		1.00
$2.6 \times 10^{-1}$ – $3.2 \times 10^{-1}$	$0^{+0.2}_{-0}$	$0^{+0.2}_{-0}$		1.00
$3.2 \times 10^{-1}$ – $4.1 \times 10^{-1}$	$0^{+0.3}_{-0}$	$0^{+0.3}_{-0}$		1.00
$5.1 \times 10^{-1}$ – $6.4 \times 10^{-1}$	$0^{+9.0 \times 10^{-2}}_{-0}$	$0^{+9.0 \times 10^{-2}}_{-0}$		1.00
$6.4 \times 10^{-1}$ – $8.0 \times 10^{-1}$	$0^{+0.1}_{-0}$	$0^{+0.1}_{-0}$		1.00

**Table 2**  
1.4 mm Differential Counts

Flux Range (Jy)	$dN/dS$ Total ( $\text{Jy}^{-1} \text{ deg}^{-2}$ )	$dN/dS$ Sync ( $\text{Jy}^{-1} \text{ deg}^{-2}$ )	$dN/dS$ Dust ( $\text{Jy}^{-1} \text{ deg}^{-2}$ )	Completeness
$1.1 \times 10^{-2}$ – $1.4 \times 10^{-2}$	$(6.93^{+3.0}_{-2.5}) \times 10^1$	$(2.48^{+2.0}_{-1.0}) \times 10^1$	$(3.96^{+2.5}_{-1.5}) \times 10^1$	0.84
$1.4 \times 10^{-2}$ – $1.7 \times 10^{-2}$	$(4.42^{+1.7}_{-1.7}) \times 10^1$	$(2.04^{+1.0}_{-1.0}) \times 10^1$	$(2.38^{+1.0}_{-1.4}) \times 10^1$	0.97
$1.7 \times 10^{-2}$ – $2.2 \times 10^{-2}$	$(2.66^{+1.1}_{-1.1}) \times 10^1$	$(1.59^{+0.8}_{-0.8}) \times 10^1$	$(1.06^{+0.8}_{-0.5}) \times 10^1$	1.00
$2.2 \times 10^{-2}$ – $2.7 \times 10^{-2}$	$(1.69^{+0.8}_{-0.6}) \times 10^1$	$(1.06^{+0.6}_{-0.6}) \times 10^1$	$6.35^{+6.4}_{-4.2}$	1.00
$2.7 \times 10^{-2}$ – $3.4 \times 10^{-2}$	$8.45^{+6.8}_{-3.4}$	$5.07^{+5.1}_{-3.4}$	$3.38^{+3.4}_{-3.4}$	1.00
$3.4 \times 10^{-2}$ – $4.2 \times 10^{-2}$	$5.39^{+4.0}_{-2.7}$	$2.70^{+4.0}_{-1.3}$	$1.35^{+2.7}_{-1.3}$	1.00
$4.2 \times 10^{-2}$ – $5.3 \times 10^{-2}$	$5.38^{+3.2}_{-3.2}$	$4.30^{+3.2}_{-2.2}$	$0^{+1.1}_{-0}$	1.00
$5.3 \times 10^{-2}$ – $6.7 \times 10^{-2}$	$2.58^{+1.7}_{-1.7}$	$2.58^{+1.7}_{-1.7}$		1.00
$6.7 \times 10^{-2}$ – $8.3 \times 10^{-2}$	$0^{+1.4}_{-0}$	$0^{+1.4}_{-0}$		1.00
$8.3 \times 10^{-2}$ – $1.0 \times 10^{-1}$	$(5.47^{+5.5}_{-5.5}) \times 10^{-1}$	$(5.47^{+5.5}_{-5.5}) \times 10^{-1}$		1.00
$1.0 \times 10^{-1}$ – $1.3 \times 10^{-1}$	$0^{+0.9}_{-0}$	$0^{+0.9}_{-0}$		1.00
$1.3 \times 10^{-1}$ – $1.6 \times 10^{-1}$	$0^{+0.3}_{-0}$	$0^{+0.3}_{-0}$		1.00
$1.6 \times 10^{-1}$ – $2.1 \times 10^{-1}$	$0^{+0.6}_{-0}$	$0^{+0.6}_{-0}$		1.00
$2.1 \times 10^{-1}$ – $2.6 \times 10^{-1}$	$0^{+0.2}_{-0}$	$0^{+0.2}_{-0}$		1.00
$2.6 \times 10^{-1}$ – $3.2 \times 10^{-1}$	$0^{+0.2}_{-0}$	$0^{+0.2}_{-0}$		1.00
$5.1 \times 10^{-1}$ – $6.4 \times 10^{-1}$	$0^{+0.2}_{-0}$	$0^{+0.2}_{-0}$		1.00

fall into the dust counts in 30% of the resamplings and into the synchrotron counts 70% of the resamplings.

We also estimate purity in each flux bin of the counts statistics using the resampled catalogs. The purity is not evaluated for the flux at the bin center (which represents an intrinsic flux), but is instead related to the S/N of the raw flux of the sources that contribute to that bin. In each resampling, if a source lies in a flux bin, we find the associated purity from its raw S/N. The purity in the bin is then the weighted average of the purity of each source detection that contributes to the bin. In the counts

presented here, the purity in the lowest flux bin is 0.80 at 2.0 mm and 0.76 at 1.4 mm.

The Bayesian method accounts for a particular sense of the purity which is slightly different than purity presented in Section 3.3.2. In Section 3.3.2, we take purity to be the fraction of noise fluctuations that are counted as sources. In principle, one would then suppress this fraction of the counts because it represents spurious detection. The outlook of the Bayesian method is that each pixel always has some intrinsic source flux—it may just be a tiny flux on top of a large positive noise

**Table 3**  
2.0 mm Cumulative Counts

Flux Range (Jy) (Jy)	$N(>S)$ Total (deg <sup>-2</sup> )	$N(>S)$ Sync (deg <sup>-2</sup> )	$N(>S)$ Dust (deg <sup>-2</sup> )	Purity
$4.4 \times 10^{-3}$ – $5.6 \times 10^{-3}$	$1.90^{+0.2}_{-0.2}$	$1.65^{+0.2}_{-0.2}$	$(2.47^{+0.7}_{-0.6}) \times 10^{-1}$	0.80
$5.6 \times 10^{-3}$ – $7.0 \times 10^{-3}$	$1.43^{+0.1}_{-0.1}$	$1.29^{+0.1}_{-0.1}$	$(1.39^{+0.5}_{-0.5}) \times 10^{-1}$	0.92
$7.0 \times 10^{-3}$ – $8.7 \times 10^{-3}$	$1.08^{+0.1}_{-0.1}$	$1.00^{+0.1}_{-0.1}$	$(6.92^{+4.6}_{-2.3}) \times 10^{-2}$	0.99
$8.7 \times 10^{-3}$ – $1.1 \times 10^{-2}$	$(8.30^{+1.0}_{-1.0}) \times 10^{-1}$	$(7.84^{+1.0}_{-0.9}) \times 10^{-1}$	$(3.46^{+2.3}_{-2.3}) \times 10^{-2}$	1.00
$1.1 \times 10^{-2}$ – $1.4 \times 10^{-2}$	$(6.57^{+0.9}_{-0.9}) \times 10^{-1}$	$(6.46^{+0.8}_{-0.9}) \times 10^{-1}$	$(1.15^{+1.2}_{-1.2}) \times 10^{-2}$	1.00
$1.4 \times 10^{-2}$ – $1.7 \times 10^{-2}$	$(5.42^{+0.8}_{-0.8}) \times 10^{-1}$	$(5.42^{+0.8}_{-0.8}) \times 10^{-1}$	$0^{+1.2 \times 10^{-2}}_{-0}$	1.00
$1.7 \times 10^{-2}$ – $2.2 \times 10^{-2}$	$(4.27^{+0.8}_{-0.7}) \times 10^{-1}$	$(4.27^{+0.8}_{-0.7}) \times 10^{-1}$		1.00
$2.2 \times 10^{-2}$ – $2.7 \times 10^{-2}$	$(3.34^{+0.7}_{-0.6}) \times 10^{-1}$	$(3.34^{+0.7}_{-0.6}) \times 10^{-1}$		1.00
$2.7 \times 10^{-2}$ – $3.4 \times 10^{-2}$	$(2.54^{+0.6}_{-0.5}) \times 10^{-1}$	$(2.54^{+0.6}_{-0.5}) \times 10^{-1}$		1.00
$3.4 \times 10^{-2}$ – $4.2 \times 10^{-2}$	$(2.08^{+0.5}_{-0.5}) \times 10^{-1}$	$(2.08^{+0.5}_{-0.5}) \times 10^{-1}$		1.00
$4.2 \times 10^{-2}$ – $5.3 \times 10^{-2}$	$(1.85^{+0.5}_{-0.5}) \times 10^{-1}$	$(1.85^{+0.5}_{-0.5}) \times 10^{-1}$		1.00
$5.3 \times 10^{-2}$ – $6.7 \times 10^{-2}$	$(1.38^{+0.5}_{-0.3}) \times 10^{-1}$	$(1.38^{+0.5}_{-0.3}) \times 10^{-1}$		1.00
$6.7 \times 10^{-2}$ – $8.3 \times 10^{-2}$	$(9.23^{+3.5}_{-3.5}) \times 10^{-2}$	$(9.23^{+3.5}_{-3.5}) \times 10^{-2}$		1.00
$8.3 \times 10^{-2}$ – $1.0 \times 10^{-1}$	$(6.92^{+2.3}_{-2.3}) \times 10^{-2}$	$(6.92^{+2.3}_{-2.3}) \times 10^{-2}$		1.00
$1.0 \times 10^{-1}$ – $1.3 \times 10^{-1}$	$(5.77^{+2.3}_{-2.3}) \times 10^{-2}$	$(5.77^{+2.3}_{-2.3}) \times 10^{-2}$		1.00
$1.3 \times 10^{-1}$ – $1.6 \times 10^{-1}$	$(4.61^{+2.3}_{-2.3}) \times 10^{-2}$	$(4.61^{+2.3}_{-2.3}) \times 10^{-2}$		1.00
$1.6 \times 10^{-1}$ – $2.1 \times 10^{-1}$	$(3.46^{+2.3}_{-2.3}) \times 10^{-2}$	$(3.46^{+2.3}_{-2.3}) \times 10^{-2}$		1.00
$2.1 \times 10^{-1}$ – $2.6 \times 10^{-1}$	$(3.46^{+1.2}_{-2.3}) \times 10^{-2}$	$(3.46^{+2.3}_{-2.3}) \times 10^{-2}$		1.00
$2.6 \times 10^{-1}$ – $3.2 \times 10^{-1}$	$(2.31^{+1.2}_{-1.2}) \times 10^{-2}$	$(2.31^{+1.2}_{-1.2}) \times 10^{-2}$		1.00
$3.2 \times 10^{-1}$ – $4.1 \times 10^{-1}$	$(1.15^{+2.3}_{-1.2}) \times 10^{-2}$	$(1.15^{+2.3}_{-1.2}) \times 10^{-2}$		1.00
$4.1 \times 10^{-1}$ – $5.1 \times 10^{-1}$	$(1.15^{+1.2}_{-1.2}) \times 10^{-2}$	$(1.15^{+1.2}_{-1.2}) \times 10^{-2}$		1.00
$5.1 \times 10^{-1}$ – $6.4 \times 10^{-1}$	$(1.15^{+1.2}_{-1.2}) \times 10^{-2}$	$(1.15^{+1.2}_{-1.2}) \times 10^{-2}$		1.00
$6.4 \times 10^{-1}$ – $8.0 \times 10^{-1}$	$0^{+2.3 \times 10^{-2}}_{-0}$	$0^{+2.3 \times 10^{-2}}_{-0}$		1.00

**Note.** The reported purity is the weighted average of the purity of source detections that contribute to a bin, see Section 5.

**Table 4**  
1.4 mm Cumulative Counts

Flux Range (Jy) (Jy)	$N(>S)$ Total (deg <sup>-2</sup> )	$N(>S)$ Sync (deg <sup>-2</sup> )	$N(>S)$ Dust (deg <sup>-2</sup> )	Purity
$1.1 \times 10^{-2}$ – $1.4 \times 10^{-2}$	$(8.39^{+1.2}_{-1.1}) \times 10^{-1}$	$(4.99^{+0.9}_{-0.8}) \times 10^{-1}$	$(3.37^{+0.8}_{-0.8}) \times 10^{-1}$	0.76
$1.4 \times 10^{-2}$ – $1.7 \times 10^{-2}$	$(6.38^{+1.0}_{-0.9}) \times 10^{-1}$	$(4.18^{+0.8}_{-0.7}) \times 10^{-1}$	$(2.20^{+0.6}_{-0.6}) \times 10^{-1}$	0.86
$1.7 \times 10^{-2}$ – $2.2 \times 10^{-2}$	$(4.84^{+0.8}_{-0.8}) \times 10^{-1}$	$(3.46^{+0.7}_{-0.6}) \times 10^{-1}$	$(1.38^{+0.5}_{-0.5}) \times 10^{-1}$	0.96
$2.2 \times 10^{-2}$ – $2.7 \times 10^{-2}$	$(3.69^{+0.7}_{-0.7}) \times 10^{-1}$	$(2.77^{+0.7}_{-0.6}) \times 10^{-1}$	$(8.07^{+4.6}_{-2.3}) \times 10^{-2}$	1.00
$2.7 \times 10^{-2}$ – $3.4 \times 10^{-2}$	$(2.65^{+0.6}_{-0.6}) \times 10^{-1}$	$(2.19^{+0.6}_{-0.5}) \times 10^{-1}$	$(4.61^{+3.5}_{-2.3}) \times 10^{-2}$	1.00
$3.4 \times 10^{-2}$ – $4.2 \times 10^{-2}$	$(1.96^{+0.6}_{-0.5}) \times 10^{-1}$	$(1.85^{+0.5}_{-0.5}) \times 10^{-1}$	$(2.31^{+1.2}_{-2.3}) \times 10^{-2}$	1.00
$4.2 \times 10^{-2}$ – $5.3 \times 10^{-2}$	$(1.50^{+0.5}_{-0.3}) \times 10^{-1}$	$(1.50^{+0.5}_{-0.5}) \times 10^{-1}$	$0^{+1.2 \times 10^{-2}}_{-0}$	1.00
$5.3 \times 10^{-2}$ – $6.7 \times 10^{-2}$	$(9.23^{+4.6}_{-3.5}) \times 10^{-2}$	$(9.23^{+4.6}_{-3.5}) \times 10^{-2}$		1.00
$6.7 \times 10^{-2}$ – $8.3 \times 10^{-2}$	$(6.92^{+2.3}_{-3.5}) \times 10^{-2}$	$(6.92^{+2.3}_{-3.5}) \times 10^{-2}$		1.00
$8.3 \times 10^{-2}$ – $1.0 \times 10^{-1}$	$(5.77^{+2.3}_{-2.3}) \times 10^{-2}$	$(5.77^{+2.3}_{-2.3}) \times 10^{-2}$		1.00
$1.0 \times 10^{-1}$ – $1.3 \times 10^{-1}$	$(4.61^{+2.3}_{-2.3}) \times 10^{-2}$	$(4.61^{+2.3}_{-2.3}) \times 10^{-2}$		1.00
$1.3 \times 10^{-1}$ – $1.6 \times 10^{-1}$	$(3.46^{+2.3}_{-2.3}) \times 10^{-2}$	$(3.46^{+2.3}_{-2.3}) \times 10^{-2}$		1.00
$1.6 \times 10^{-1}$ – $2.1 \times 10^{-1}$	$(2.31^{+2.3}_{-1.2}) \times 10^{-2}$	$(2.31^{+2.3}_{-1.2}) \times 10^{-2}$		1.00
$2.1 \times 10^{-1}$ – $2.6 \times 10^{-1}$	$(2.31^{+1.2}_{-1.2}) \times 10^{-2}$	$(2.31^{+1.2}_{-1.2}) \times 10^{-2}$		1.00
$2.6 \times 10^{-1}$ – $3.2 \times 10^{-1}$	$(1.15^{+2.3}_{-1.2}) \times 10^{-2}$	$(1.15^{+2.3}_{-1.2}) \times 10^{-2}$		1.00
$3.2 \times 10^{-1}$ – $4.1 \times 10^{-1}$	$(1.15^{+1.2}_{-1.2}) \times 10^{-2}$	$(1.15^{+1.2}_{-1.2}) \times 10^{-2}$		1.00
$4.1 \times 10^{-1}$ – $5.1 \times 10^{-1}$	$(1.15^{+1.2}_{-1.2}) \times 10^{-2}$	$(1.15^{+1.2}_{-1.2}) \times 10^{-2}$		1.00
$5.1 \times 10^{-1}$ – $6.4 \times 10^{-1}$	$(1.15^{+1.2}_{-1.2}) \times 10^{-2}$	$(1.15^{+1.2}_{-1.2}) \times 10^{-2}$		1.00

fluctuation and so is not strictly a false detection. When we determine the counts, we draw such sub-threshold fluxes from the posterior flux distribution. The effect of this is that in some

fraction of the bootstrap samples, a source will scatter downward in flux (representing a tiny intrinsic flux plus a large positive noise fluctuation), out of the flux range presented. No additional

correction for the purity (in the sense of Section 3.3.2) needs to be applied. Completeness is not included in this framework and so is corrected for explicitly.

## 6. ASSOCIATIONS WITH EXTERNAL CATALOGS AND FOLLOW-UP OBSERVATIONS WITH ATCA

Where possible, we identify candidate counterparts to the SPT-detected sources in several external catalogs and databases. We have queried the NED<sup>31</sup> and SIMBAD<sup>32</sup> databases for counterparts within 2' of all 3496 of our  $\geq 3\sigma$  sources. We have also searched catalogs from five individual observatories for counterparts: (1) the SUMSS catalog; (2) the *IRAS-FSC*; (3) the RASS-BSC and RASS-FSC; (4) the PMN catalog; and (5) the AT20G catalog. We search these catalogs, in particular, because these observatories are especially relevant for extragalactic sources in the southern hemisphere. Additionally, as mentioned in Section 3.3.2, we have performed follow-up observations at 6 cm on many of our brightest sources with the ATCA.

ATCA observations were performed at 6 cm, 12 mm, and 7 mm during 2008 August under program C1563. At 6 cm, 55 sources in this field were observed and 52 sources were detected at a typical rms noise of 0.5 mJy. We classify one of the sources not detected (SPT-S J053250–5047.1) as a dusty source (see Section 7.2). The other two undetected sources (SPT-S J053412–5924.3 and SPT-S J055232–5349.4) are extended in the SUMSS catalog (45'' resolution) and thus heavily resolved at the typical  $9'' \times 3''$  6 cm resolution.

The majority of our synchrotron-dominated sources have a clear counterpart either in an external catalog, in our 6 cm ATCA observations, or both. Because these sources are expected to have fluxes that vary significantly over time (Kellermann & Pauliny-Toth 1968), and because the radio catalogs in which we search for counterparts are not significantly deeper than our own measurements, one might expect to not find counterparts for sources that were caught at peak brightness in the SPT observations.

Despite this caveat, of the 107 sources above  $5\sigma$  that we classify as synchrotron dominated, only three of them do not have SUMSS counterparts within 30''. The brightest of these three sources (SPT-S J053345–5818.1) is classified as extended using the method of Section 3.5 and we find counterparts for this source within 10'' in both the PMN catalog and our ATCA follow-up observations. The extended nature of this source and the offset between the SUMSS and SPT/PMN/ATCA positions for this source are expected if this source is an AGN with extended jets. The synchrotron emission from the source is presumably dominated by the radio-lobe (jet) contribution in the 36 cm SUMSS observations but dominated by emission from the core at shorter wavelengths. This frequency-dependent core-to-lobe flux ratio is commonly seen in radio-loud AGNs (e.g., Kharb et al. 2008; De Zotti et al. 2010) and is predicted by certain unified AGN models (e.g., Jackson & Wall 1999). Indeed, visual inspection of this source reveals one SUMSS source on either side of the SPT location (each within 40'') and a RASS-BSC object (also presumably dominated by emission from the AGN core) directly on top of the SPT location.

Of the remaining two  $\geq 5\sigma$  synchrotron-dominated sources with no SUMSS counterpart within 30'', one (SPT-S J050334–5244.8) has a SUMSS counterpart and a counterpart in our ATCA follow-up, both within 35'', and the other

(SPT-S J053726–5434.4) has a counterpart 11'' away in the Véron-Cetty & Véron (2006) and Hamburg-ESO (Wisotzki et al. 1991) catalogs as well as a possibly associated SUMSS source 1/3 away. We thus believe that each of the sources that we detect at  $\geq 5\sigma$  and classify as synchrotron-dominated is a real source. This is consistent with our estimates of purity in Section 3.3.2, which predict a false detection rate of effectively zero above  $5\sigma$ .

The situation with our dust-dominated sources is very different. Of the 23 (47) sources above  $5\sigma$  ( $4.5\sigma$ ) that we classify as dust dominated, only 10 (12) have counterparts (in any catalog) within 30'', and only 12 (15) have counterparts within 1'. Given the studies summarized in Section 3.3.2 and the counterparts found for the synchrotron-dominated sources, there is almost no chance that all (or even a majority of) these detections without counterparts are spurious. Of the dust-dominated sources above  $5\sigma$  that do have counterparts within 30'', all but three are nearby galaxies detected with *IRAS*. Two of the remaining three are associated with SUMSS sources, while the other is SPT-S J054716–5104.1 which is associated with the debris disk around the star  $\beta$  Pictoris. In this field, there are no other SPT sources within 30'' of a SIMBAD database star.

## 7. INDIVIDUAL-POPULATION SOURCE COUNTS AND IMPLICATIONS

To briefly summarize the results of the last several sections, three broad classes of point sources are detected with high significance in the SPT 1.4 mm and 2.0 mm maps:

1. Sources with 1.4–2.0 mm flux ratios consistent with synchrotron emission, the vast majority of which appear in radio catalogs and/or in our centimeter-wave follow-up observations with ATCA and which we generically refer to as AGNs.
2. Sources with 1.4–2.0 mm flux ratios consistent with dust emission which have low-redshift ( $z \ll 1$ ) counterparts in the *IRAS-FSC*, and which we will generically call *IRAS* sources.
3. Previously undetected sources with 1.4–2.0 mm flux ratios consistent with dust emission.

Here, we present the measured source counts as a function of flux for each of these populations and discuss the implications of our measurements.

### 7.1. Synchrotron-dominated Source Counts

From associations with radio catalogs and from our 6 cm follow-up observations with ATCA, we conclude that SPT sources with 1.4–2.0 mm spectral indices less than 1.66 are consistent with being members of the classical radio-source population (see De Zotti et al. 2010 for a recent review). Although contributions to this population can come from synchrotron and free-free emission in normal and starburst galaxies (Condon 1992; De Zotti et al. 2010), the population is dominated at short radio wavelengths (30 cm and below) and moderate to high fluxes (10 mJy–1 Jy) by synchrotron emission from AGNs (De Zotti et al. 2010). At even shorter wavelengths (1 cm and below), the moderate-to-high-flux counts are expected to be dominated by the sub-class of AGNs known as flat-spectrum radio quasars (FSRQs; De Zotti et al. 2005).

The behavior of this source population at mm wavelengths is interesting for several reasons. Astrophysically, mm measurements of AGNs have the potential to inform models of AGN emission mechanisms and evolution, particularly whether

<sup>31</sup> <http://nedwww.ipac.caltech.edu/>

<sup>32</sup> <http://simbad.u-strasbg.fr/simbad>

FSRQs undergo spectral steepening at shorter wavelengths. This short-wavelength behavior of FSRQs is also of interest to the CMB and SZ communities, as the predictions of contamination of mm CMB power spectrum measurements and SZ galaxy cluster surveys by AGN emission depend heavily on extrapolations of long-wavelength source properties to mm wavelengths (Lin & Mohr 2007; Reichardt et al. 2009). Finally, the compact angular size of FSRQs (along with their short-wavelength brightness) make them attractive candidates for phase calibration sources for the Atacama Large Millimeter Array (ALMA).

Two obvious questions that can be addressed with multi-band SPT observations of classical radio sources are as follows. (1) Are the sources selected at 2.0 mm consistent with a population of FSRQs? (2) Is the spectral behavior of these sources between 2.0 mm and 1.4 mm consistent with their longer-wavelength (flat-spectrum) behavior, or is there evidence of a spectral break or turnover?

The first question is made somewhat ambiguous by the lack of a clear definition of the FSRQ population in terms of synchrotron spectral index. De Zotti et al. (2005) use a single spectral index of  $\alpha = -0.1$  for their model of the FSRQ population, while surveys targeting “flat spectrum radio sources” have generally chosen  $\alpha \geq -0.4$  or  $-0.5$  as the defining threshold (Jackson et al. 2002; Healey et al. 2007). Nevertheless, we can ask whether the behavior of these sources between 2.0 mm and longer wavelengths is more consistent with a mean spectral index such as De Zotti et al. (2005) use or with a value more typical of steep-spectrum sources such as  $\alpha \sim -0.8$  (De Zotti et al. 2010).

We investigate this question using two lines of evidence. First, we have the comparison of the 2.0 mm SPT flux with fluxes measured at longer wavelengths. A serious caveat to any comparison of non-simultaneous observations of radio sources is that the known variability of such sources will add scatter—and, potentially, bias—to estimates of spectral behavior. Our ATCA 6 cm follow-up observations took place approximately 2 months after the SPT observations, which will limit the effect of variability on our 6 cm-to-2.0 mm comparisons to timescales shorter than this separation. According to Murphy et al. (2010), the AT20G observations of sources between  $-60^\circ$  and  $-50^\circ$  decl. took place in 2005 September and October, so 1.5 cm-to-2.0 mm comparisons should be viewed with greater caution.

With this caveat in mind, we find that our highest-significance 2.0 mm-selected, synchrotron-dominated sources are completely consistent with flat spectral behavior (or  $\alpha \sim -0.1$ ) between 6 cm and 2.0 mm. If we take the 57 sources for which we have robust ( $\geq 5\sigma$ ) detections at both 6 cm and 2.0 mm, and we calculate a single spectral index for each source using the best-fit 2.0 mm flux from Table 5 and the raw 6 cm flux, we find that these sources have a distribution of spectral indices characterized by  $\alpha = -0.13 \pm 0.21$ . Because this sample of 57 sources is not purely 2.0 mm selected (we are omitting sources without a robust 6 cm detection) and because the 6 cm data have not been corrected for flux boosting, one might worry that this result is biased toward high 6 cm fluxes and, hence, steeper spectral indices. If we repeat the calculation using only the top 10 brightest 2.0 mm sources—which are all detected above  $50\sigma$  at 6 cm—we find a spectral index distribution of  $\alpha = -0.08 \pm 0.22$ .

The second line of evidence that supports the hypothesis that our 2.0 mm selected, synchrotron-dominated sources are FSRQs—or, more specifically, have a mean spectral index near

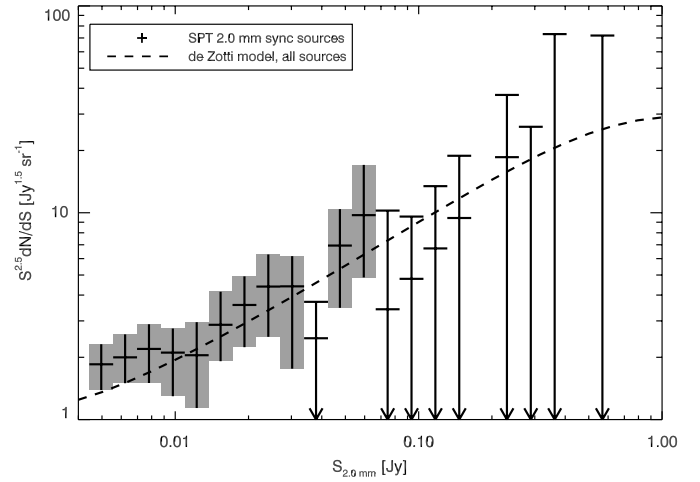


**Figure 10.** Differential counts for the population of sources identified as synchrotron-dominated compared to the De Zotti et al. (2005) model. Here the counts are scaled by  $S^{2.5}$  relative to by-band differential counts shown in Figure 9 to match the (geometrical) convention in AGN literature. The error regions enclose 68% of the probability centered about the median counts and are calculated using the bootstrap over the two-band posterior intrinsic flux (at 2.0 mm) that is described in Section 5. In these counts, a source is identified as synchrotron dominated if  $\alpha < 1.66$  in the resampling.

$\bar{\alpha} = -0.1$ —is the agreement between the 2.0 mm synchrotron-dominated counts and the predictions of De Zotti et al. (2005). The De Zotti et al. (2005) model includes contributions from many populations of radio sources, including normal and star-forming galaxies and many types of AGNs, but at 1 cm and below, the  $>10$  mJy model counts are dominated by FSRQs. Figure 10 compares our synchrotron-dominated 2.0 mm counts to the De Zotti et al. (2005) 2 mm model. The model is roughly consistent with our measured counts, indicating that the 2.0 mm synchrotron-dominated counts are consistent with a power-law extrapolation of the long-wavelength FSRQ counts, and that the spectral behavior used to extrapolate the long-wavelength FSRQ counts in the model—in this case, simply assuming  $\alpha = -0.1$  for all FSRQs—is reasonably accurate down to 2.0 mm.

The answer to the second question—whether the radio sources selected at 2.0 mm show flat spectral behavior all the way to 1.4 mm—is addressed by our simultaneous 1.4 mm and 2.0 mm observations of these sources. These observations indicate that a mean spectral index of  $\bar{\alpha} = -0.1$  is not an accurate description of the spectral behavior of these sources between 1.4 mm and 2.0 mm. The distribution of spectral indices in Figure 8 shows that our synchrotron-dominated sources have 1.4 mm-to-2.0 mm spectral indices peaked around  $\alpha = -0.5$ , and a similar result is found for the sum of the posterior spectral index PDFs for the 57 sources detected above  $5\sigma$  at both 6 cm and 2.0 mm. If we take the ten brightest 2.0 mm selected sources, we find that the sum of the posterior spectral index PDFs of these sources is inconsistent with  $\alpha = -0.1$  at 97%.

Interestingly, if we perform the same calculation using the published 1.5 cm AT20G fluxes for our top ten 2.0 mm selected sources, the 2.0 mm-to-1.5 cm spectral index distribution is  $\alpha = -0.31 \pm 0.29$  while the 1.5 cm-to-6 cm spectral index distribution is  $\alpha = 0.25 \pm 0.36$ —i.e., there is some evidence that the flux of these sources peaks between 6 cm and 2.0 mm. Biases induced by source variability are unlikely to have a significant effect on this measurement for two reasons. First, these sources are so far above the detection threshold at 2.0 mm that they

**Table 5**  
Point Sources Above  $4.5\sigma$  at 1.4 mm or 2.0 mm in an  $87 \text{ deg}^2$  SPT Field Centered at R.A.  $5^{\text{h}}30^{\text{m}}$ , decl.  $-55^\circ$  (J2000)

ID and Coordinates:			2.0 mm data:			1.4 mm data:			Spectral Index and Type:				Nearest Source in		
SPT ID	R.A. (deg)	Decl. (deg)	S/N	$S^{\text{raw}}$ (mJy)	$S^{\text{dist}}$ (mJy)	S/N	$S^{\text{raw}}$ (mJy)	$S^{\text{dist}}$ (mJy)	$\alpha^{\text{raw}}$	$\alpha^{\text{dist}}$	$P(\alpha > 1.66)$	Type	SUMSS (arcsec)	RASS (arcsec)	IRAS (arcsec)
SPT-S J045913–5942.4	74.804	–59.708	6.20	7.51	$7.26^{+1.27}_{-1.27}$	7.05	22.58	$20.85^{+3.90}_{-4.02}$	3.0	$2.9^{+0.7}_{-0.7}$	0.95	dust	43	575	815
SPT-S J050000–5752.5	75.000	–57.875	44.01	53.28	$52.99^{+2.50}_{-2.50}$	15.15	48.52	$47.80^{+5.39}_{-5.39}$	–0.3	$-0.3^{+0.3}_{-0.3}$	0.00	sync	3	313	486
SPT-S J050003–5229.0	75.015	–52.485	5.33	6.70	$5.91^{+1.38}_{-1.47}$	2.15	7.20	$5.57^{+2.88}_{-2.47}$	0.2	$0.0^{+1.4}_{-1.7}$	0.08	sync	18	923	1979
SPT-S J050019–5321.3	75.081	–53.356	39.42	49.52	$49.26^{+2.32}_{-2.41}$	10.82	36.21	$35.52^{+4.64}_{-4.64}$	–0.9	$-0.9^{+0.3}_{-0.4}$	0.00	sync	4	627	189
SPT-S J050211–5040.7	75.546	–50.679	6.76	8.86	$8.15^{+1.40}_{-1.41}$	1.15	3.98	$4.71^{+2.51}_{-1.48}$	–2.2	$-1.5^{+1.2}_{-1.0}$	0.00	sync	7	1184	1459
SPT-S J050321–5328.3	75.839	–53.472	5.56	6.98	$6.16^{+1.36}_{-1.45}$	1.43	4.77	$4.35^{+2.64}_{-1.70}$	–1.0	$-0.9^{+1.5}_{-1.4}$	0.03	sync	8	694	1312
SPT-S J050329–5735.6 <sup>a</sup>	75.874	–57.595	45.35	54.90	$54.60^{+2.57}_{-2.57}$	16.43	52.62	$51.83^{+5.76}_{-5.66}$	–0.1	$-0.1^{+0.3}_{-0.3}$	0.00	sync	2	1058	583
SPT-S J050334–5244.8 <sup>b</sup>	75.892	–52.747	5.96	7.49	$6.80^{+1.35}_{-1.38}$	1.95	6.51	$5.43^{+2.86}_{-2.19}$	–0.4	$-0.5^{+1.3}_{-1.5}$	0.02	sync	32	581	1611
SPT-S J050401–5023.2	76.006	–50.387	40.49	53.07	$52.79^{+2.49}_{-2.49}$	12.50	43.27	$42.54^{+5.17}_{-5.27}$	–0.6	$-0.6^{+0.3}_{-0.3}$	0.00	sync	1	998	1301
SPT-S J050424–5711.9	76.100	–57.199	16.05	20.17	$19.94^{+1.47}_{-1.52}$	7.56	25.28	$24.53^{+4.08}_{-4.08}$	0.6	$0.6^{+0.4}_{-0.5}$	0.00	sync	11	158	493

**Notes.**

- <sup>a</sup> Extended source; see Section 3.5.  
<sup>b</sup> No SUMSS source within  $30''$ , but SUMSS source and ATCA detection within  $35''$ ; see Section 6.  
<sup>c</sup> Associated with NGC 1824; see Section 3.5.  
<sup>d</sup> Near deep SZ decrement but not spurious; see Section 6.  
<sup>e</sup> Offset between 1.4 mm and 2.0 mm emission; see Section 3.5.  
<sup>f</sup> Associated with NGC 1853; see Section 3.5.  
<sup>g</sup> Possibly spurious detection from sidelobe of strong SZ decrement; see Section 6.  
<sup>h</sup> Chance superposition ( $45''$  separation) of SUMSS source and new dust-dominated detection; see Section 3.5.  
<sup>i</sup> Two SUMSS sources within  $35''$ ; see Section 6.  
<sup>j</sup> No SUMSS source within  $1'$ , but associated with HE 0536-5435 [VCV2001]; see Section 6.  
<sup>k</sup> Associated with  $\beta$  Pictoris; see Section 6.  
<sup>l</sup> Associated with ESO 160-G 002; see Section 3.5.

(This table is available in its entirety in a machine-readable form in the online journal. A portion is shown here for guidance regarding its form and content.)

would have been significant detections at any epoch. Second, biases due to variability would tend to drive estimates of this spectral index in the opposite direction—because sources are likely to be selected at their peak brightness, measurements taken at any other epoch should produce systematically lower fluxes. This implies that if we had 1.5 cm measurements taken simultaneously with the SPT measurements, we would tend to find even higher 1.5 cm fluxes than in the AT20G catalog (assuming the variability is simultaneous at the two wavelengths). These arguments imply that the evidence for these sources’ flux peaking between 6 cm and 2.0 mm is fairly robust, if not overly statistically significant.

## 7.2. Dust-dominated Source Counts

### 7.2.1. The Dust-dominated Assumption, Spectral Indices, and Self-absorbed Synchrotron

We have referred throughout this work to the population of sources with 1.4 mm-to-2.0 mm spectral indices greater than 1.66 as “dust-dominated.” For the sources in this class that have *IRAS*-FSC counterparts, the assumption that thermal emission from dust is the dominant mechanism at mm wavelengths is reasonable given their large IR fluxes. The 1.4 mm-to-2.0 mm spectral indices for these sources are consistent with dust emission—the sum of the posterior spectral index PDFs for the five brightest sources with *IRAS* counterparts peaks at  $\alpha = 3.2$ —and comparisons of 1.4 mm SPT fluxes and 100  $\mu\text{m}$  *IRAS* fluxes of these sources show that their emission is consistent with thermal dust at moderate temperatures (20–40 K) from the mm through the far-IR (see Section 7.2.2 and Figure 11 for details).

While thermal dust emission is also the most natural candidate for explaining the sources with 1.4 mm-to-2.0 mm spectral indices greater than 1.66 that do not have *IRAS*-FSC counterparts, we cannot a priori rule out self-absorbed synchrotron emission from AGNs as the dominant emission mechanism for these sources. Self-absorbed synchrotron is the leading emission model for the population of gigahertz-peaked-spectrum (GPS) radio sources (see O’Dea 1998 for a review), and it is the only emission mechanism other than thermal emission from dust that could plausibly produce 1.4 mm-to-2.0 mm spectral indices well above 0. As the name suggests, GPS sources typically peak around wavelengths of 30 cm (e.g., Stanghellini et al. 1998), but GPS sources have been observed with peaks at wavelengths as short as 1 cm (Edge et al. 1998), and there is no fundamental physics that rules out self-absorbed synchrotron emission peaking at much shorter wavelengths. However, several lines of reasoning suggest that the  $\alpha > 1.66$  sources without *IRAS*-FSC counterparts are not dominated by self-absorbed synchrotron.

The first argument against GPS radio sources as the explanation for our “dust-dominated” counts without *IRAS*-FSC counterparts is that their spectral behavior is too steep even for self-absorbed synchrotron, while it is perfectly consistent with thermal dust emission. Stanghellini et al. (1998) show that, even well longward of the peak wavelength, the mean spectral index of GPS sources is  $\alpha \sim 0.8$ , and rarely do they find spectral indices as high as 2.0. In contrast, the sum of the posterior spectral index PDFs for the brightest five dust-dominated sources without *IRAS* counterparts peaks at  $\alpha = 3.3$  and is inconsistent with  $\alpha = 2.0$  at 97% confidence. This peak value of  $\alpha = 3.3$  is consistent (within the width of the two distributions) with the peak of  $\alpha = 3.2$  for the top five sources with *IRAS*-FSC counterparts, sources which we are confident are truly dust-dominated. The

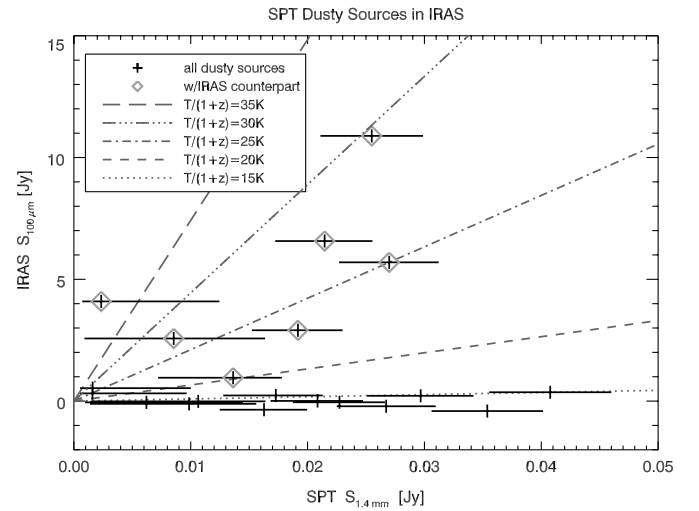


**Figure 11.** *IRAS* 100  $\mu\text{m}$  flux vs. SPT 1.4 mm flux for all SPT dust-dominated sources at  $S/N > 5$ . *IRAS* flux is taken from a version of the ISSA (Wheelock et al. 1994) 100  $\mu\text{m}$  map which has been filtered to enhance point-source  $S/N$ . Horizontal error bars are the 68% enclosed interval in the posterior 1.4 mm flux distribution (as in Table 5). Vertical error bars are the width of the noise distribution in the filtered *IRAS* map. SPT sources with counterparts within  $1'$  in the *IRAS* FSC are shown with diamond symbols. Lines of constant 100  $\mu\text{m}$ –1.4 mm flux ratio are shown for five emission models, all modified blackbody laws with a dust emissivity index of  $\beta = 1.5$  (consistent with the value of  $\beta$  used in Dunne & Eales 2001, Chapman et al. 2005, and Kovács et al. 2006) and with dust temperatures of 15, 20, 25, 30, and 35 K (if the emitter is nearby) or those temperatures times  $1+z$  (if the emitter lies at redshift  $z$ ). There is a clear distinction between the locus of sources with *IRAS*-FSC counterparts—which have flux ratios consistent with warm, low-redshift dust emission—and the points that lie along the  $x$ -axis and have no counterparts, which must be either at moderate to high redshift or have anomalously cold dust.

peak value of these  $\alpha$  distributions are also consistent with the best-fit mean spectral index of  $\bar{\alpha} = 3.7 \pm 0.2$  found by Hall et al. (2010) for Poisson-distributed sources below the SPT detection threshold—the vast majority of which are expected to be dust dominated. Interestingly, all of these peak  $\alpha$  values are actually steeper than typical values predicted by models for spectral indices of dust-dominated sources (e.g., Lagache et al. 2004), a point discussed in detail in Hall et al. (2010).

Another argument against the GPS explanation for these sources is the lack of radio and X-ray counterparts. Siemiginowska et al. (2008) found that GPS sources have 2–10 keV fluxes of up to  $10^{46}$  erg  $\text{s}^{-1}$ , easily detectable in the RASS, and our brightest “dust-dominated” sources would have to be almost an order of magnitude dimmer at 36 cm than at 1.4 mm to evade detection in SUMSS. Finally, Kellermann & Pauliny-Toth (1981) argue that the peak wavelength of a GPS source should be proportional to flux density to the  $-0.4$  power, meaning that sources that peak at mm wavelengths should be 2.5 orders of magnitude brighter than sources that peak at cm wavelengths, so they should be much rarer as well. Based on this set of arguments, we conclude that our sources with 1.4 mm-to-2.0 mm spectral indices greater than 1.66 are indeed dominated by thermal dust emission.

### 7.2.2. SPT Dust-dominated Source Counts and Arguments for a New Population of mm Sources

One might presume that the dust-dominated sources presented here are exact analogs to the submm-selected SMG population measured by SCUBA and other instruments. However, SMG source counts at 850  $\mu\text{m}$  are found to drop precipitously at

flux levels above 5–10 mJy (e.g., Coppin et al. 2006). Assuming an average spectral index of  $\alpha = 2.8$  (the estimate for mean SMG spectral index from Knox et al. 2004), this drop in the counts would occur at  $\sim 2$  mJy at 1.4 mm, leading one to expect a 1.4 mm survey to see very few SMGs above the  $\sim 10$  mJy level needed for a robust detection in the SPT 1.4 mm band. Indeed, extrapolating two of the models used to fit SCUBA counts in Coppin et al. (2006) to 1.4 mm and 10 mJy indicates that there should be  $\ll 1$  SMG above 10 mJy at 1.4 mm in the SPT 87 deg<sup>2</sup> field; a similar extrapolation of the Schechter function fit to the AzTEC 1.1 mm counts in Austermann et al. (2010) yields a similar prediction. Using a spectral index closer to the mean of the dust-dominated part of the distribution shown in Figure 8 would drive these predictions even lower. Quite contrary to these predictions, SPT detects 20 dust-dominated sources above 10 mJy at 1.4 mm, including 9 above 20 mJy. What are these sources if not SMGs?

One possibility is that they are nearby ULIRGs, the low-redshift analogues of SMGs. These sources are rare enough to not contribute significantly to the submm counts estimated from very small patches of sky. As noted in Section 6, a fraction of the bright dust-dominated sources detected by the SPT have counterparts in the *IRAS-FSC*, and most of these sources are indeed low-redshift ULIRGs. The majority of SPT dust-dominated sources, however, do not have *IRAS-FSC* counterparts, or counterparts in any existing catalog. Likewise, in deep ( $\sim 24.4$  AB mag) *griz* optical data taken by the Blanco Cosmology Survey (BCS<sup>33</sup>; which encompass roughly half of the 87 deg<sup>2</sup> described here) there are no obvious counterparts.

It is unlikely that these sources are just below the threshold for inclusion in *IRAS-FSC*, given that the brightest three SPT dust-dominated sources do not have *IRAS-FSC* counterparts. Figure 11 makes an even stronger argument that these sources are a very different population than the SPT sources with *IRAS-FSC* counterparts. This figure shows a scatter plot of *IRAS* 100  $\mu$ m flux—estimated from an *IRAS* Sky Survey Atlas (ISSA, Wheelock et al. 1994) 100  $\mu$ m map filtered to enhance point-source S/N—versus SPT 1.4 mm flux.<sup>34</sup> The sources with and without *IRAS-FSC* counterparts occupy clearly distinct loci of points. The sources with *IRAS-FSC* counterparts are consistent with nearby sources that have typical dust temperatures of 25–35 K (Dunne & Eales 2001), while the sources without *IRAS-FSC* counterparts have ISSA 100  $\mu$ m flux consistent with zero and thus must either be at moderate to high redshift or have anomalously cold dust ( $\lesssim 15$  K). A stacking analysis of the 13 objects classified as dust-dominated with 1.4 mm S/N greater than 4.5 and no *IRAS-FSC* counterpart shows that these sources have mean *IRAS* 100  $\mu$ m flux of 15.9 mJy, with a  $2\sigma$  upper limit for that mean of 106 mJy. These same sources have mean 1.4 mm flux of 18 mJy. If we assume an Arp220 SED for these sources, this stacking analysis implies these sources lie at a mean redshift of  $\langle z \rangle = 3.1$ , with a  $2\sigma$  lower limit of  $\langle z \rangle = 2.0$ . Assuming a modified blackbody spectrum with  $\beta = 1.5$ , we obtain a  $2\sigma$  upper limit of the combination of dust temperature and redshift of  $T_d/(1+z) = 14.3$  K, implying a  $2\sigma$  lower limit on mean redshift of  $\langle z \rangle = 1.1$  if  $T_d = 30$  K.

The mean dust temperature of high redshift SMGs measured from previous work is  $\sim 35$  K (Chapman et al. 2005; Kovács et al. 2006), but there have been detections of a few galaxies with dust temperatures  $\sim 20$  K (e.g., Kovács et al. 2006). There

is expected to be both a hot ( $\sim 40$  K) dust component from the ISM surrounding actively star-forming regions with many young stars, as well as a cold ( $\sim 20$  K) dust component surrounding the diffuse quiescently evolving population of old red stars (Dunne & Eales 2001; Vlahakis et al. 2005; Coppin et al. 2008). *IRAS* would be largely insensitive to the cold dust component, which might explain why these SPT sources escaped previous detection. However, given the brightness of these objects, if these sources were galaxies at  $z < 1$  then we would expect to see them in BCS, Digitized Sky Survey,<sup>35</sup> or Two Micron All Sky Survey images,<sup>36</sup> and we do not. This test depends on the assumption of a particular SED for the galaxies, but the most pessimistic galaxy SED assumption—namely, an Arp220-like SED with a high mm-to-optical brightness ratio—still predicts that such objects would be detected in the optical and near-IR (NIR).

Throughout this work, we have assumed that the majority of sources detected in the mm waveband by the SPT have been of extragalactic origin, as this field is at high galactic latitude and has explicitly been chosen for its low contamination by galactic cirrus. How robust of a statement can be made as to the extragalactic nature on the dusty sources not detected in any external catalog? A similar question was posed in Lawrence (2001) and it was demonstrated that the majority of SCUBA sources could not be of galactic origin. The SPT sources cannot be galactic H II regions as the accompanying free-free emission would have been detected by low-frequency radio catalogs such as PMN and SUMSS. They could be nearby, cold ( $T_d < 10$  K), pre-star-forming clouds in the galaxy similar to sources described in Désert et al. (2008). However, as this field is at high galactic latitude and the clouds would presumably be located in the galactic disk and not the halo, the sources would therefore be nearby (within  $\sim 1$  kpc). Since these clouds are expected to be parsec-scale objects (Egan et al. 1998), they would have an angular extent ( $\sim 5'$ ) much larger than the SPT beam and would be obviously detected by eye in the unfiltered map. We have also tested the dark cloud hypothesis by measuring optical extinction along the lines of sight toward the SPT dusty sources. A comparison of the optical color distribution of BCS objects toward dust-dominated sources to the colors toward random directions in the field shows no excess extinction at the positions of these sources. Although we cannot definitively confirm that *none* of these sources are of galactic origin, these tests demonstrate that they are predominantly extragalactic.

Comparisons of SPT dust-dominated source counts with model predictions strengthen the conclusion that our bright, dust-dominated sources without *IRAS* counterparts are a new, possibly high-redshift and lensed, population. Figure 12 shows the cumulative SPT dust-dominated counts versus flux and predictions from three models. Lagache et al. (2004), Negrello et al. (2007), and Pearson & Khan (2009) make predictions for counts at or very near our 1.4 mm band. All three models have two basic components: moderate-to-high-redshift starburst galaxies (which account for basically all the counts seen by SCUBA at 850  $\mu$ m) and nearby galaxies (including the LIRGs and ULIRGs seen in *IRAS*). The Negrello et al. (2007) model also includes a component of the high-redshift starburst population which has been strongly lensed by foreground galaxies. At first glance, all models agree fairly well with the SPT counts at 1.4 mm. However, the counts at fluxes above

<sup>33</sup> <http://cosmology.illinois.edu/BCS/>

<sup>34</sup> We chose to plot the *IRAS* 100  $\mu$ m channel (as opposed to 60  $\mu$ m) because it is the closest band to the SED peak and to the SPT 1.4 mm band.

<sup>35</sup> <http://cadwww.dao.nrc.ca/cadcbn/getdss>

<sup>36</sup> <http://irsa.ipac.caltech.edu/applications/2MASS/>

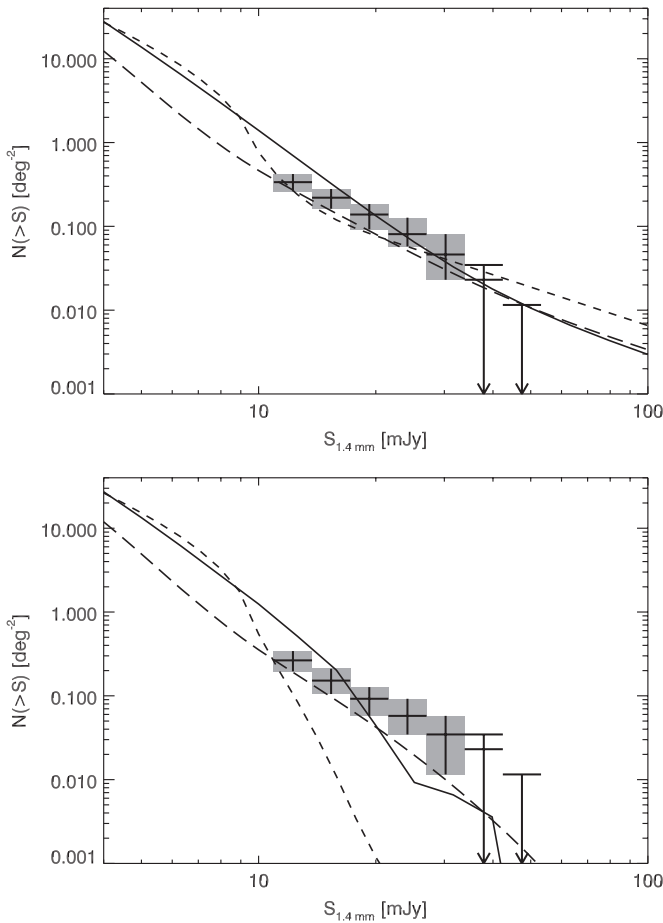


**Figure 12.** Cumulative SPT dust-dominated source counts vs. 1.4 mm flux, with models overplotted. Model curves are as follows: short dashed line, Lagache et al. (2004) 1.38 mm prediction; long dashed line, Negrello et al. (2007) 1.4 mm prediction; dot-dashed line, Pearson & Khan (2009) 1.38 mm prediction. The error regions enclose 68% of the probability centered about the median counts and are calculated using the bootstrap over the two-band posterior intrinsic flux (at 1.4 mm) that is described in Section 5. In these counts, a source is identified as dust dominated if  $\alpha \geq 1.66$  in the resampling. Top panel: this plot shows counts and models with all dust-dominated sources included. Bottom panel: this plot shows counts calculated excluding sources that have *IRAS*-FSC counterparts (within  $1'$ ) and models calculated excluding populations that should be detectable in the *IRAS*  $60 \mu\text{m}$  band above the typical FSC limit of 0.2 Jy. The SPT detects sources in excess of what is predicted by the models shown once the *IRAS* sources have been removed.

10–20 mJy are dominated in all models by sources that should be detectable in the *IRAS*-FSC above the  $60 \mu\text{m}$  flux cut of 200 mJy, while our measured counts are dominated by sources without *IRAS*-FSC counterparts. We have modified the publicly available Lagache et al. (2004) code to exclude such sources from their model,<sup>37</sup> and Pearson & Khan (2009) and Negrello et al. (2007) have supplied us with model counts excluding sources with  $60 \mu\text{m}$  flux greater than 200 mJy. We then recalculate our 1.4 mm dust-dominated counts excluding sources with *IRAS*-FSC counterparts and compare these modified counts to the modified predictions in the bottom panel of Figure 12.

There are significant discrepancies between our measured counts without *IRAS* counterparts and the Lagache et al. (2004) and Pearson & Khan (2009) model predictions in both the

slope of the counts and the number of sources above 20 mJy. The Negrello et al. (2007) model also under-predicts the SPT counts but the shape of the counts are in good agreement. A modest adjustment along either axis would bring the model into excellent agreement. As stated above, the main difference between the Negrello et al. (2007) model and the Lagache et al. (2004) and Pearson & Khan (2009) models is the inclusion of a population of high redshift, strongly lensed dusty star-forming galaxies.

Among the possible explanations for this new population, the hypothesis that these sources are at high redshift is particularly compelling. The longer-wavelength SPT observations will be sensitive to a higher-redshift population than the submm surveys (due to the stronger negative  $K$ -correction), and there is considerable evidence that the very brightest SMGs are at the highest redshifts (Ivison et al. 2002; Pope et al. 2005; Greve et al. 2008). This empirically observed trend of SMG brightness with redshift is plausible both because more distant systems have a higher probability of being gravitationally lensed (Blain 1996; Blain et al. 1999) and because evolution in star formation as a function of environment, called “cosmic downsizing,” is consistent with a higher star formation rate in massive systems at high redshift (Cowie et al. 1996; Cole et al. 2000). Models exist in the literature that predict the existence of a mm/submm-bright population similar to ours resulting from both lensing (Blain 1996; Perrotta et al. 2003; Negrello et al. 2007) and intrinsically luminous high- $z$  sources (Devriendt et al. 2010). The reason that such objects would have been missed by previous mm/submm instruments is simply that SPT surveys so much more area (87  $\text{deg}^2$  for this small subset of the SPT survey to  $\sim 1 \text{deg}^2$  for the total area surveyed by SCUBA) and is hence much more likely to find rare, bright systems (due to strong lensing or intrinsic luminosity) that a smaller survey might miss.

If this subset of the SPT-identified dusty sources are indeed at high redshift, they represent an intriguing new class of mm sources, whether they are strongly lensed or intrinsically ultra-luminous. Strongly lensed systems allow observers to detect fainter background sources at higher redshift than would otherwise be obtainable. Because lensing is achromatic, these sources will be brighter at all wavelengths, facilitating detailed studies which have otherwise been difficult to achieve. Equally exciting would be the identification of high-redshift galaxies which are more massive and forming stars more prodigiously than any systems yet identified. The identification of such galaxies would be a strong test of models of galaxy formation and evolution. Regardless of whether the sources are lensed or intrinsically luminous, a sample of high-redshift, dust-enshrouded star-forming galaxies has the potential to be a useful tool for the study of very early epochs of star and galaxy formation.

## 8. CONCLUSIONS

The SPT has detected 188 sources above  $4.5\sigma$  (over 3000 above  $3\sigma$ ) in two-band data over a small (87  $\text{deg}^2$ ) subset of the full survey region. This is the first survey of its kind at mm wavelengths and mJy flux levels, both in survey area—the 87  $\text{deg}^2$  presented here is over an order of magnitude more area than previous mm surveys at these flux levels—and in the ability to spectrally discriminate between different source populations. Some of the sources detected in this work appear to be members of a new and intriguing population of dust-enshrouded, star-forming galaxies.

We use the ratio of flux in the 1.4 mm and 2.0 mm bands to estimate the spectral index for every detected source. Using the

<sup>37</sup> Using the template SED models supplied by Lagache et al. (2004), we find that any source detected at  $>10$  mJy at 1.4 mm below redshift  $z = 0.2$  should have  $60 \mu\text{m}$  flux above 200 mJy, so our modification to their model is effectively just a redshift cut at  $z = 0.2$ .

posterior PDF for this spectral index, we classify each source as either synchrotron dominated or dust dominated. At high flux levels (above  $\sim 15$  mJy) in both bands, the majority of sources we detect are synchrotron-dominated; the synchrotron-dominated population continues to dominate the 2.0 mm counts down to the detection threshold, but the dust-dominated sources begin to take over the 1.4 mm counts near the 15 mJy level.

The synchrotron-dominated sources we detect are consistent with the population of radio sources that is well established from radio and cm surveys. All of our  $>5\sigma$  sources in this class have a clear counterpart in existing radio catalogs. The number counts as a function of 2.0 mm flux that we derive for this population are consistent with the predictions of De Zotti et al. (2005). Spectral comparisons within the SPT data and with ATCA data at 6 cm (taken in follow-up observations) and 1.5 cm (Murphy et al. 2010) show that the synchrotron-dominated sources we detect are consistent with FSRQs (as predicted), but that the flat-spectrum behavior has turned over by mm wavelengths. This conclusion is important for AGN models and for predictions of radio source contamination in CMB and SZ measurements.

A fraction of our dust-dominated sources have counterparts in the *IRAS*-FSC and are typically associated with low-redshift ( $z \ll 1$ ) ULIRGs. The majority of our dust-dominated sources, however, have no counterpart in existing catalogs, and we argue that they represent a new and exciting population of mm sources. Comparisons of source counts for this population with model predictions and *IRAS* limits on the 100  $\mu\text{m}$  flux of these sources demonstrate that these sources are inconsistent with either simple extrapolations of the submm-selected population at lower fluxes or with low-redshift galaxies with normal dust properties. Further, the mm-wavelength selection of such high-flux sources over a large survey area suggests a high-redshift population. Possibilities for explaining this new family of sources include strong lensing of dimmer background sources, ultra-luminous starburst galaxies at moderate-to-high redshift, and ( $z \sim 1$ ) galaxies with extremely cold dust. Comparisons to models favor the hypothesis for these sources being strongly lensed. Any one of these explanations would have interesting implications for models of star and galaxy formation and be of potential cosmological interest. Properly locating these sources in the broader context of the IR/submm/mm galaxy population is a major challenge for future work. An extensive program to determine the SEDs, morphologies, and redshift distribution of these objects is underway. Multi-wavelength follow-up imaging facilities such as the *Hubble Space Telescope*, the *Spitzer Space Telescope*, the *Herschel Space Observatory*, and the ALMA, will be crucial to disentangling the various possibilities and uncovering the nature of these objects.

The point source results presented here use only a small fraction of the complete SPT data set. SPT is continuing to take data and has already observed 800  $\text{deg}^2$  to similar depths as this work at 1.4 and 2.0 mm. 600  $\text{deg}^2$  of this area also has 3.2 mm coverage. The complete SPT survey is expected to cover over 2000  $\text{deg}^2$  with these three wavelengths and will produce a catalog containing thousands of additional sources.

We thank A. Blain and M. Malkan for advice and guidance, C. Lacey, G. Lagache, M. Negrello, C. Pearson, and G. De Zotti for providing us with their models, and the anonymous referee for useful suggestions.

The SPT team gratefully acknowledges the contributions to the design and construction of the telescope by S. Busetti, E. Chauvin, T. Hughes, P. Huntley, and E. Nichols and his team of

iron workers. We also thank the National Science Foundation (NSF) Office of Polar Programs, the United States Antarctic Program and the Raytheon Polar Services Company for their support of the project. We are grateful for professional support from the staff of the South Pole station. We thank C. Greer, T. Lanting, J. Leong, W. Lu, M. Runyan, D. Schwan, and M. Sharp for their early contributions to the SPT project, and J. Joseph and C. Vu for their contributions to the electronics. We acknowledge S. Alam, W. Barkhouse, S. Bhattacharya, L. Buckley-Geer, S. Hansen, H. Lin, Y-T Lin, A. Rest, C. Smith, and D. Tucker for their contribution to BCS data acquisition.

The SPT is supported by the NSF through grants ANT-0638937 and ANT-0130612. Partial support is also provided by the NSF Physics Frontier Center grant PHY-0114422 to the Kavli Institute of Cosmological Physics (KICP) at the University of Chicago, the Kavli Foundation and the Gordon and Betty Moore Foundation. The McGill group acknowledges funding from the National Sciences and Engineering Research Council of Canada, the Quebec Fonds de recherche sur la nature et les technologies, and the Canadian Institute for Advanced Research. The following individuals acknowledge additional support: B.S. from the Brinson Foundation, B.A.B., K.K.S., and E.R.S. from a KICP Fellowship, J.M. from a Fermi Fellowship, Z.S. from a GAAN Fellowship, and A.T.L. from the Miller Institute for Basic Research in Science, University of California Berkeley. N.W.H. acknowledges support from an Alfred P. Sloan Research Fellowship. A.A.S. and W.W. received grant support from the Smithsonian Institution Office of the Under Secretary for Science. Support for M.B. was provided by the W. M. Keck Foundation.

This research has made use of the SIMBAD database, operated at CDS, Strasbourg, France, the NASA/IPAC Extragalactic Database (NED) which is operated by the Jet Propulsion Laboratory, California Institute of Technology, under contract with the National Aeronautics and Space Administration, and the NASA/IPAC Infrared Science Archive, which is operated by the Jet Propulsion Laboratory, California Institute of Technology, under contract with the National Aeronautics and Space Administration. This research used the facilities of the Canadian Astronomy Data Centre operated by the National Research Council of Canada with the support of the Canadian Space Agency. The ATCA is part of the Australia Telescope, which is funded by the Commonwealth of Australia for operation as a national facility managed by the CSIRO. Some of the results in this paper have been derived using the HEALPix (Górski et al. 2005) package. We acknowledge the use of the Legacy Archive for Microwave Background Data Analysis (LAMBDA). Support for LAMBDA is provided by the NASA Office of Space Science.

## REFERENCES

- Aretxaga, I., et al. 2007, *MNRAS*, 379, 1571  
 Austermann, J. E., et al. 2010, *MNRAS*, 401, 160  
 Bai, L., et al. 2007, *ApJ*, 664, 181  
 Barger, A. J., Cowie, L. L., Sanders, D. B., Fulton, E., Taniguchi, Y., Sato, Y., Kawara, K., & Okuda, H. 1998, *Nature*, 394, 248  
 Barnes, J. E., & Hernquist, L. E. 1991, *ApJ*, 370, L65  
 Bertoldi, F., et al. 2007, *ApJS*, 172, 132  
 Blain, A. W. 1996, *MNRAS*, 283, 1340  
 Blain, A. W., Chapman, S. C., Smail, I., & Ivison, R. 2004, *ApJ*, 611, 725  
 Blain, A. W., Moller, O., & Maller, A. H. 1999, *MNRAS*, 303, 423  
 Blain, A. W., Smail, I., Ivison, R. J., Kneib, J.-P., & Frayer, D. T. 2002, *Phys. Rep.*, 369, 111  
 Borys, C., Chapman, S., Halpern, M., & Scott, D. 2003, *MNRAS*, 344, 385  
 Caputi, K. I., et al. 2007, *ApJ*, 660, 97

- Carlstrom, J. E., et al. 2009, *PASP*, submitted (arXiv:0907.4445)
- Chapin, E. L., et al. 2009, *MNRAS*, **398**, 1793
- Chapman, S. C., Blain, A. W., Smail, I., & Ivison, R. J. 2005, *ApJ*, **622**, 772
- Coble, K., et al. 2007, *AJ*, **134**, 897
- Cole, S., Lacey, C. G., Baugh, C. M., & Frenk, C. S. 2000, *MNRAS*, **319**, 168
- Condon, J. J. 1992, *ARA&A*, **30**, 575
- Coppin, K., Halpern, M., Scott, D., Borys, C., & Chapman, S. 2005, *MNRAS*, **357**, 1022
- Coppin, K., et al. 2006, *MNRAS*, **372**, 1621
- Coppin, K., et al. 2008, *MNRAS*, **384**, 1597
- Cowie, L. L., Songaila, A., Hu, E. M., & Cohen, J. G. 1996, *AJ*, **112**, 839
- Crawford, T. M., Switzer, E. R., Holzappel, W. L., Reichardt, C. L., Marrone, D. P., & Vieira, J. D. 2010, *ApJ*, **718**, 513
- De Zotti, G., Massardi, M., Negrello, M., & Wall, J. 2010, *A&AR*, **18**, 1
- De Zotti, G., Ricci, R., Mesa, D., Silva, L., Mazzotta, P., Toffolatti, L., & González-Nuevo, J. 2005, *A&A*, **431**, 893
- Désert, F., et al. 2008, *A&A*, **481**, 411
- Devlin, M. J., et al. 2009, *Nature*, **458**, 737
- Devriendt, J., et al. 2010, *MNRAS*, **403**, L84
- Draine, B. T. 2003, *ARA&A*, **41**, 241
- Dunne, L., & Eales, S. A. 2001, *MNRAS*, **327**, 697
- Dwek, E., et al. 1998, *ApJ*, **508**, 106
- Dye, S., et al. 2009, *ApJ*, **703**, 285
- Eddington, A. S. 1913, *MNRAS*, **73**, 359
- Edge, A. C., Pooley, G., Jones, M., Grainge, K., & Saunders, R. 1998, in *ASP Conf. Ser. 144, IAU Colloq. 164: Radio Emission from Galactic and Extragalactic Compact Sources*, ed. J. A. Zensus, G. B. Taylor, & J. M. Wrobel (San Francisco, CA: ASP), 187
- Egan, M. P., Shipman, R. F., Price, S. D., Carey, S. J., Clark, F. O., & Cohen, M. 1998, *ApJ*, **494**, L199
- Górski, K. M., Hivon, E., Banday, A. J., Wandelt, B. D., Hansen, F. K., Reinecke, M., & Bartelmann, M. 2005, *ApJ*, **622**, 759
- Greve, T. R., Ivison, R. J., Bertoldi, F., Stevens, J. A., Dunlop, J. S., Lutz, D., & Carilli, C. L. 2004, *MNRAS*, **354**, 779
- Greve, T. R., Pope, A., Scott, D., Ivison, R. J., Borys, C., Conzelice, C. J., & Bertoldi, F. 2008, *MNRAS*, **389**, 1489
- Greve, T. R., et al. 2005, *MNRAS*, **359**, 1165
- Hall, N. R., et al. 2010, *ApJ*, **718**, 632
- Healey, S. E., Romani, R. W., Taylor, G. B., Sadler, E. M., Ricci, R., Murphy, T., Ulvestad, J. S., & Winn, J. N. 2007, *ApJS*, **171**, 61
- Hincks, A. D., et al. 2010, *ApJ*, in press (arXiv:0907.0461)
- Hinshaw, G., et al. 2009, *ApJS*, **180**, 225
- Högbom, J. A. 1974, *A&AS*, **15**, 417
- Holland, W. S., et al. 1999, *MNRAS*, **303**, 659
- Hughes, D. H., et al. 1998, *Nature*, **394**, 241
- Ivison, R. J., et al. 2002, *MNRAS*, **337**, 1
- Ivison, R. J., et al. 2007, *MNRAS*, **380**, 199
- Jackson, C. A., & Wall, J. V. 1999, *MNRAS*, **304**, 160
- Jackson, C. A., Wall, J. V., Shaver, P. A., Kellermann, K. I., Hook, I. M., & Hawkins, M. R. S. 2002, *A&A*, **386**, 97
- Kellermann, K. I., & Pauliny-Toth, I. I. K. 1968, *ARA&A*, **6**, 417
- Kellermann, K. I., & Pauliny-Toth, I. I. K. 1981, *ARA&A*, **19**, 373
- Kharb, P., O'Dea, C. P., Baum, S. A., Daly, R. A., Mory, M. P., Donahue, M., & Guerra, E. J. 2008, *ApJS*, **174**, 74
- Knox, L., Holder, G. P., & Church, S. E. 2004, *ApJ*, **612**, 96
- Kovács, A., Chapman, S. C., Dowell, C. D., Blain, A. W., Ivison, R. J., Smail, I., & Phillips, T. G. 2006, *ApJ*, **650**, 592
- Lagache, G., Puget, J.-L., & Dole, H. 2005, *ARA&A*, **43**, 727
- Lagache, G., et al. 2004, *ApJS*, **154**, 112
- Laurent, G. T., et al. 2005, *ApJ*, **623**, 742
- Lawrence, A. 2001, *MNRAS*, **323**, 147
- Le Floc'h, E., et al. 2005, *ApJ*, **632**, 169
- Lin, Y., & Mohr, J. J. 2007, *ApJS*, **170**, 71
- Lueker, M., et al. 2010, *ApJ*, in press (arXiv:0912.4317)
- Mason, B. S., Weintraub, L., Sievers, J., Bond, J. R., Myers, S. T., Pearson, T. J., Readhead, A. C. S., & Shepherd, M. C. 2009, *ApJ*, **704**, 1433
- Mauch, T., Murphy, T., Buttery, H. J., Curran, J., Hunstead, R. W., Piestrzynski, B., Robertson, J. G., & Sadler, E. M. 2003, *MNRAS*, **342**, 1117
- Moshir, M., Kopman, G., & Conrow, T. A. O. 1992, *IRAS Faint Source Survey, Explanatory Supplement Version 2* (Pasadena, CA: Infrared Processing and Analysis Center, California Institute of Technology)
- Murphy, T., et al. 2010, *MNRAS*, **402**, 2403
- Narayanan, D., Hayward, C. C., Cox, T. J., Hernquist, L., Jonsson, P., Younger, J. D., & Groves, B. 2010, *MNRAS*, **401**, 1613
- Negrello, M., Perrotta, F., González-Nuevo, J., Silva, L., De Zotti, G., Granato, G. L., Baccigalupi, C., & Danese, L. 2007, *MNRAS*, **377**, 1557
- O'Dea, C. P. 1998, *PASP*, **110**, 493
- Padin, S., et al. 2008, *Appl. Opt.*, **47**, 4418
- Patanchon, G., et al. 2009, *ApJ*, **707**, 1750
- Pearson, C., & Khan, S. A. 2009, *MNRAS*, **399**, L11
- Perera, T. A., et al. 2008, *MNRAS*, **391**, 1227
- Perrotta, F., Magliocchetti, M., Baccigalupi, C., Bartelmann, M., De Zotti, G., Granato, G. L., Silva, L., & Danese, L. 2003, *MNRAS*, **338**, 623
- Plagge, T., et al. 2010, *ApJ*, **716**, 1118
- Pope, A., Borys, C., Scott, D., Conzelice, C., Dickinson, M., & Mobasher, B. 2005, *MNRAS*, **358**, 149
- Pope, A., et al. 2006, *MNRAS*, **370**, 1185
- Reichardt, C. L., et al. 2009, *ApJ*, **694**, 1200
- Rieke, G. H., & Lebofsky, M. J. 1979, *ARA&A*, **17**, 477
- Sadler, E. M., Ricci, R., Ekers, R. D., Sault, R. J., Jackson, C. A., & De Zotti, G. 2008, *MNRAS*, **385**, 1656
- Sanders, D. B., & Mirabel, I. F. 1996, *ARA&A*, **34**, 749
- Scott, K. S., et al. 2008, *MNRAS*, **385**, 2225
- Scott, S. E., et al. 2002, *MNRAS*, **331**, 817
- Sehgal, N., Bode, P., Das, S., Hernandez-Monteagudo, C., Huffenberger, K., Lin, Y., Ostriker, J. P., & Trac, H. 2010, *ApJ*, **709**, 920
- Shaw, L. D., Zahn, O., Holder, G. P., & Doré, O. 2009, *ApJ*, **702**, 368
- Siemiginowska, A., LaMassa, S., Aldcroft, T. L., Bechtold, J., & Elvis, M. 2008, *ApJ*, **684**, 811
- Smail, I., Ivison, R. J., & Blain, A. W. 1997, *ApJ*, **490**, L5
- Stanghellini, C., O'Dea, C. P., Dallacasa, D., Baum, S. A., Fanti, R., & Fanti, C. 1998, *A&AS*, **131**, 303
- Staniszewski, Z., et al. 2009, *ApJ*, **701**, 32
- Sunyaev, R. A., & Zeldovich, Y. B. 1972, *Comments Astrophys. Space Phys.*, **4**, 173
- Swinbank, A. M., et al. 2008, *MNRAS*, **391**, 420
- Swinbank, A. M., Smail, I., Chapman, S. C., Blain, A. W., Ivison, R. J., & Keel, W. C. 2004, *ApJ*, **617**, 64
- Tacconi, L. J., et al. 2006, *ApJ*, **640**, 228
- Tacconi, L. J., et al. 2008, *ApJ*, **680**, 246
- Teerikorpi, P. 2004, *A&A*, **424**, 73
- Tegmark, M., & de Oliveira-Costa, A. 1998, *ApJ*, **500**, L83
- Toffolatti, L., Negrello, M., González-Nuevo, J., De Zotti, G., Silva, L., Granato, G. L., & Argüeso, F. 2005, *A&A*, **438**, 475
- Véron-Cetty, M.-P., & Véron, P. 2006, *A&A*, **455**, 773
- Viero, M. P., et al. 2009, *ApJ*, **707**, 1766
- Vlahakis, C., Dunne, L., & Eales, S. 2005, *MNRAS*, **364**, 1253
- Voges, W., et al. 1999, *A&A*, **349**, 389
- Voges, W., et al. 2000, *VizieR Online Data Catalog*, **9029**, 0
- Voss, H., Bertoldi, F., Carilli, C., Owen, F. N., Lutz, D., Holdaway, M., Ledlow, M., & Menten, K. M. 2006, *A&A*, **448**, 823
- Weiß, A., et al. 2009, *ApJ*, **707**, 1201
- Wheelock, S. L., et al. 1994, *NASA STI/Recon Tech. Rep.*, **95**, 22539
- Wisotzki, L., Reimers, D., & Wamsteker, W. 1991, *A&A*, **247**, L17
- Wright, A. E., Griffith, M. R., Burke, B. F., & Ekers, R. D. 1994, *ApJS*, **91**, 111